Cold exposure impairs extracellular vesicle swarm–mediated nasal antiviral immunity

Di Huang, PhD,[a,b] Maie S. Taha, PhD,[a,b,c] Angela L. Nocera, PhD,[a,b] Alan D. Workman, MD,[a] Mansoor M. Amiji, PhD,[b] and Benjamin S. Bleier, MD[a] *Boston, Mass, and Cairo, Egypt*

GRAPHICAL ABSTRACT

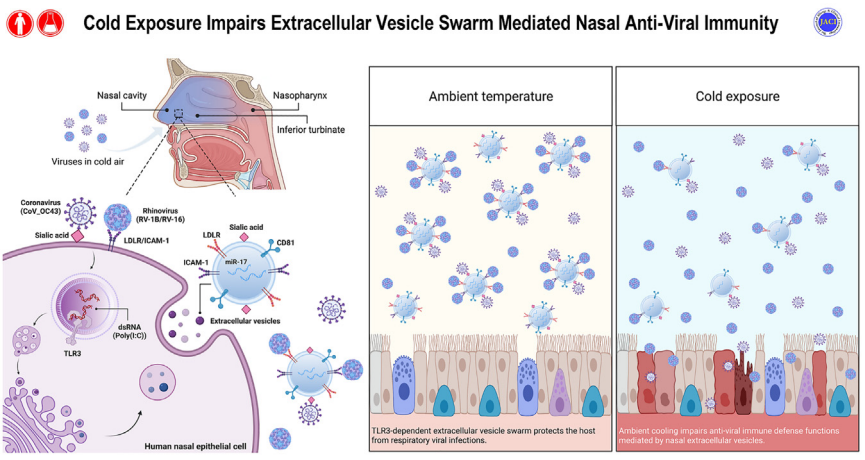

Background: The human upper respiratory tract is the first site of contact for inhaled respiratory viruses and elaborates an array of innate immune responses. Seasonal variation in respiratory viral infections and the importance of ambient temperature in modulating immune responses to infections have been well recognized; however, the underlying biological mechanisms remain understudied.

Objective: We investigated the role of nasal epithelium-derived extracellular vesicles (EVs) in innate Toll-like receptor 3 (TLR3)-dependent antiviral immunity.

Methods: We evaluated the secretion and composition of nasal epithelial EVs after TLR3 stimulation in human autologous cells and fresh human nasal mucosal surgical specimens. We also explored the antiviral activity and mechanisms of TLR3-stimulated EVs against respiratory viruses as well as the effect of cool ambient temperature on TLR3-dependent antiviral immunity.

Results: We found that polyinosinic:polycytidylic acid, aka poly(I:C), exposure induced a swarm-like increase in the secretion of nasal epithelial EVs via the TLR3 signaling. EVs participated in TLR3-dependent antiviral immunity, protecting the host from viral infections through both EV-mediated functional delivery of miR-17 and direct virion neutralization after binding to virus ligands via surface receptors, including LDLR and ICAM-1. These potent antiviral immune defense functions mediated by TLR3-stimulated EVs were impaired by cold exposure via a decrease in total EV secretion as well as diminished microRNA packaging and antiviral binding affinity of individual EV.

Conclusion: TLR3-dependent nasal epithelial EVs exhibit multiple innate antiviral mechanisms to suppress respiratory viral infections. Furthermore, our study provides a direct quantitative mechanistic explanation for seasonal variation in upper respiratory tract infection prevalence. (J Allergy Clin Immunol 2023;151:509-25.)

From [a]the Department of Otolaryngology, Massachusetts Eye and Ear Infirmary, Harvard Medical School, and [b]the Department of Pharmaceutical Sciences, School of Pharmacy, Northeastern University, Boston; and [c]the Department of Pharmaceutics and Industrial Pharmacy, Faculty of Pharmacy, Cairo University, Cairo.

Funding support was received from Northeastern University (an intramural COVID-19 research grant to M.M.A.) and the National Eye Institute of the National Institutes of Health (P30EY003790 to S.E.R.I.).

Disclosure of potential conflict of interest: The authors declare that they have no relevant conflicts of interest.

Received for publication June 23, 2022; revised August 24, 2022; accepted for publication September 20, 2022.

Available online December 6, 2022.

Corresponding author: Mansoor M. Amiji, PhD, Department of Pharmaceutical Sciences, School of Pharmacy, Northeastern University, Boston, MA 02115. E-mail: m.amiji@northeastern.edu. Or: Benjamin S. Bleier, MD, Department of Otolaryngology, Massachusetts Eye and Ear Infirmary, Harvard Medical School, Boston, MA 02114. E-mail: Benjamin_Bleier@meei.harvard.edu.

The CrossMark symbol notifies online readers when updates have been made to the article such as errata or minor corrections

0091-6749/$36.00

https://doi.org/10.1016/j.jaci.2022.09.037

Key words: *Upper airway, respiratory viruses, extracellular vesicles, TLR3 signaling pathway, innate immunity, seasonal variation*

Upper respiratory tract infections (URIs) pose a significant public health burden in terms of decreased productivity, absenteeism at work or school, and health care system overload.[1] URIs may be associated with multiple clinical sequelae, such as otitis media, sinusitis, bronchiolitis, pneumonia, and exacerbation of asthma or chronic obstructive pulmonary disease.[2] The most common causes of URIs in adults include *Picornaviridae, Coronaviridae, Orthomyxoviridae, Paramyxoviridae, Pneumoviridae,* and *Adenoviridae*.[3] These viruses may be highly evolutionarily dynamic with significant mutation rates, enabling them to evade preexisting immunity.[4] This poses a consistent risk of emergence and reemergence of unpredictable virus strains causing life-threatening epidemics and pandemics.

Seasonal variation in increased URI prevalence, morbidity, and mortality during the winter period has been well recognized.[5,6] These adverse outcomes may be further exacerbated by socioeconomic and behavioral factors as well as age, sex, and comorbidities.[7] While environmental factors appear to contribute to the epidemiologic phenomenon of seasonal variation in URIs, a clear mechanism has thus far remained elusive. Previously, many respiratory viruses were thought to cause infections primarily in the nasal cavity, consistent with the observation that some virus strains replicate better at lower temperatures than at the core body temperature.[8] Accumulating evidence suggests that temperature and humidity may independently or jointly contribute to the risk of respiratory viral infections due to changes in host susceptibility.[9,10] Similarly, recent fundamental research exploring the underlying molecular mechanisms demonstrates that cold temperature may impair host innate immune response to viral infections.[11,12]

The nasal cavity is one of the initial contact points between the external environment and the human body; it is highly sensitive to changes in ambient temperature.[13] The nasal mucosal barrier therefore represents the front line of defense against exposure to inhaled respiratory pathogens through multiple host immune mechanisms. The physical barrier function of the nasal mucosa can prevent pathogens from entering the body through the production of mucus glycoproteins,[14] mucociliary clearance,[15] and epithelial tight junctions.[16,17] The nasal epithelial cells also play important roles in the initiation, maintenance, and regulation of innate immunity. These defense mechanisms are constitutive and can be activated by both membrane-bound and cytoplasmic pattern recognition receptors that recognize pathogen-associated molecular patterns commonly found in viruses.[17] One of the best characterized classes of pattern recognition receptors is the Toll-like receptor (TLR) family, which are transmembrane receptors expressed on multiple cell types, including nasal epithelial cells. TLRs recognize components of invading microbes and trigger the first line of innate immune and inflammatory responses to combat infectious agents.[18] Within the TLR family, TLR3 is considered a major mediator of cellular defense to viral infection, as it responds to double-stranded RNA (dsRNA), a common by-product of virus replication.[19]

While these strategies occur at the level of the epithelial cell, recent evidence has shown that active host mucosal defense to bacteria extends into the mucus itself through the epithelial release of antimicrobial extracellular vesicle (EV) swarms.[20] EVs are lipid-bound vesicles secreted by cells into the extracellular space and have been reported in virtually all human biological fluids, including blood, lymph, and nasal mucus.[21,22] Depending on the cell of origin, EVs can carry diverse constituents, such as nucleic acids, proteins, lipids, amino acids, and metabolites.[23] Accumulating evidence has shown that in addition to their previously described antibacterial role,[20] EVs may also regulate innate immune responses to viral infections.[24,25] This occurs through the functional delivery of antiviral agents, such as microRNAs (miRNAs), into neighboring or distant recipient cells.[26,27] miRNAs are small noncoding RNAs that posttranscriptionally regulate gene expression by mediating hydrolysis and translational inhibition of target messenger RNAs (mRNAs).[28] Previous studies have reported that several miRNAs have direct antiviral effects or regulate the inflammatory pathways, thereby enhancing antiviral immunity against infections.[29-31] In addition to transport of antiviral agents between cells, EVs can also exert direct virion neutralization by binding to virus ligands via surface receptors and block their entry to host cells.[32]

In light of the recent evidence regarding the role of EV swarms in epithelial antibacterial defense, we hypothesized first that EVs also participate in innate nasal mucosal TLR3-dependent antiviral immunity through both functional delivery of antiviral miRNAs and direct binding of mucus-suspended virions, and second that these functions are impaired by cold air conditions via a decrease in total EV secretion as well as reduced miRNA packaging and antiviral binding affinity of individual EV. To test these hypotheses, we first analyzed the *in vitro* antiviral activity mediated by

Abbreviations used

Anti–miR-NC:	Random sequence miRNA inhibitor negative control
BEBM:	Bronchial epithelial basal medium
BEGM:	Bronchial epithelial growth medium
BSA:	Bovine serum albumin
DAPI:	4′,6-Diamidino-2-phenylindole
dsRNA:	Double-stranded RNA
ELISA:	Enzyme-linked immunosorbent assay
EV:	Extracellular vesicle
HNEpC:	Human nasal epithelial cell
ICAM-1:	Intercellular adhesion molecule 1
LDLR:	Low-density lipoprotein receptor
miRNA:	MicroRNA
mRNA:	Messenger RNA
MTS:	3-(4,5-Dimethylthiazol-2-yl)-5-(3-carboxymethoxyphenyl)-2-(4-sulfophenyl)-2*H*-tetrazolium
NANA:	*N*-Acetylneuraminic acid
PBS:	Phosphate-buffered saline
Poly(I:C):	Polyinosinic:polycytidylic acid
qPCR:	Real-time quantitative PCR
RV:	Rhinovirus
SARS-CoV:	Severe acute respiratory syndrome coronavirus
siLDLR:	LDLR silencing
siNC:	Nontargeting siRNA negative control
siRNA:	Small interfering RNA
$TCID_{50}$:	Median tissue culture infective dose
TEM:	Transmission electron microscopy
TLR:	Toll-like receptor
URI:	Upper respiratory tract infection

TLR3-dependent EVs against 3 different common respiratory viruses using primary human nasal epithelial cells (HNEpCs) and identified antiviral miRNAs and surface receptor proteins associated with the antiviral function. We then measured the *in vivo* temperature reduction experienced by the anterior nasal cavity in cold ambient environments in healthy human subjects. Next, we applied a similar temperature reduction to *in vitro* cultures to investigate temperature-dependent expression profiles of miRNAs and surface receptor proteins and validated the results in a clinically relevant *ex vivo* model of live human mucosal surgical specimens. Finally, we replicated the antiviral mechanistic studies at this reduced intranasal temperature to determine the effect of cold exposure on antiviral activity mediated by TLR3-dependent EVs. This investigation is of unique clinical relevance in that all *in vitro* findings were directly validated in live human tissue. This study thereby provides a compelling quantitative mechanistic explanation for seasonal variation in URI prevalence.

METHODS

Human nasal mucosa tissue sampling

Ethics approval (protocol 2019P001204) was obtained from the Mass General Brigham institutional review board. All study participants provided informed written consent. Normal inferior turbinate mucosal tissue was collected from healthy subjects free of rhinosinusitis or allergic rhinitis and undergoing nasal airway surgery for anatomic obstruction. The patients had not been exposed to antibiotics or steroids for at least 4 weeks before sampling. Additional exclusion criteria included ciliary dysfunction, autoimmune disease, cystic fibrosis, immunodeficiency, and smoking. Surgically collected turbinate tissues were immediately obtained and placed in bronchial epithelial growth medium (BEGM; Lonza, Basel, Switzerland), then transported on ice for processing.

Live human nasal mucosa tissue culture

Normal inferior turbinate mucosal tissue of healthy subjects was dissected into 5 × 5 mm explants using Miltex biopsy punches (Integra Life Sciences, Princeton, NJ). Each explant sample was rinsed and weighed, placed into an Eppendorf tube containing 0.5 mL of culture media, and incubated at 37°C, 5% CO_2, and 95% relative humidity.

Primary human nasal epithelial cell culture

Primary HNEpCs, either purchased from PromoCell (Heidelberg, Germany) or isolated from normal nasal turbinate mucosal tissue of healthy subjects, were cultured using a procedure described previously.[20,33] Mucosal samples were washed and digested in protease from *Streptomyces griseus* (Sigma-Aldrich, St Louis, Mo) for 90 minutes at 37°C and centrifuged for 5 minutes at 1000 rpm. Cell pellets were then resuspended in BEGM and plated on petri dishes for 2 hours to remove contaminating fibroblasts. Cells were then expanded on collagen (collagen from human placenta, Bornstein and Traub Type IV; Sigma-Aldrich)-coated T-75 flasks at 37°C, 5% CO_2, and 95% relative humidity.

In vitro polyinosinic:polycytidylic acid stimulation

A TLR3 agonist polyinosinic:polycytidylic acid [poly(I:C)] was used for dose–response experiments on HNEpCs grown to 80% confluence in 96-well plates. Cells were rinsed with phosphate-buffered saline (PBS), exposed to increasing doses of poly(I:C) (0.5, 2.5, or 5 μg/mL; Sigma-Aldrich) premixed with Lipofectamine 2000 (Thermo Fisher Scientific, Waltham, Mass) in bronchial epithelial basal medium (BEBM; Lonza), and incubated for 1 hour at 37°C. Subsequently, media were replaced with fresh BEGM and cells were further incubated at 37°C. Media were collected at different time points (1, 3, 5, 7, or 24 hours), and cells were rinsed with PBS. All rinses were collected for EV isolation and cell viability after poly(I:C) stimulation was determined using a 3-(4,5-dimethylthiazol-2-yl)-5-(3-carboxymethoxyphenyl)-2-(4-sulfophenyl)-2*H*-tetrazolium (MTS) assay. HNEpCs used for EV production were grown in T-75 flasks. After 1 hour of exposure to the 2.5 μg/mL poly(I:C) dose at 37°C, media were replaced with fresh BEGM, and cells were further incubated for 24 hours at 37°C or 32°C. The secreted EVs in media were isolated, validated, and used for downstream applications as described below.

Assessment of cell viability

Cell viability after poly(I:C) stimulation was determined using an MTS assay, which is based on the mitochondrial conversion of a tetrazolium salt. Cells were exposed to increasing doses of poly(I:C) (0.5, 2.5, or 5 μg/mL) for 1 hour at 37°C, followed by replacement of fresh culture medium and continuous incubation for different periods of time (1, 3, 5, 7, or 24 hours) at 37°C. At the end point, 20 μL of CellTiter 96 AQueous One solution reagent (Promega, Madison, Wis) was added to each well in 100 μL of culture medium and incubated at 37°C for 2 hours. The absorbance was measured using a microplate reader (Synergy H1, BioTek Instruments, Winooski, Vt) at a wavelength of 490 nm with background subtraction at 680 nm.

TLR3 signaling pathway interrogation

HNEpCs grown to 80% confluence in T-75 flasks were pretreated with a TLR3/dsRNA complex inhibitor (Calbiochem, San Diego, Calif; 10 μmol, Sigma-Aldrich) alone or in a combination with an IRF3 agonist (KIN 1148, 10 μmol; Selleck Chemicals, Houston, Tex) for 2 hours at 37°C, followed by poly(I:C) stimulation as described above. After 24 hours, the intracellular protein expression of TLR3 and phospho-IRF3 was analyzed. The number of EVs secreted from cells was also quantitated.

Ex vivo poly(I:C) stimulation

Turbinate mucosal explants were immersed in 0.5 mL of BEBM and exposed to the 10 μg/mL poly(I:C) dose for 1 hour at 37°C. Media were then replaced with fresh BEGM, and explants were further incubated at 37°C or 32°C. After 24 hours, the secreted EVs in media were isolated, validated, and used for downstream applications.

EV isolation

EVs were isolated from whole mucus or culture media using the ultracentrifugation procedure described previously.[20] Samples were centrifuged for 45 minutes at 12,000 × *g* at 4°C to pellet cell debris. Supernatants were then transferred to polypropylene tubes and ultracentrifuged for 2 hours at 110,000 × *g* at 4°C. After removing the supernatants, the pellet was resuspended in PBS. The suspension was filtered through a 0.22 μm filter (Thermo Fisher) and collected in a fresh tube. The filtered suspension was then centrifuged for 70 minutes at 110,000 × *g* at 4°C. The pellet was resuspended in the buffer needed for downstream application.

Quantification of EVs

The purified EVs were quantified by measuring the level of CD81 in EVs using a CD81 exosome enzyme-linked immunosorbent assay (ELISA) complete kit (System Biosciences, Palo Alto, Calif). All values were normalized to total protein concentration within the same sample with a Pierce BCA protein assay kit (Thermo Fisher).

Characterization of EVs

The particle size and zeta potential of EVs were determined by dynamic light scattering using a Malvern Nano ZS (Malvern Instruments, Malvern, England, United Kingdom). Morphology of EVs was observed by cryogenic transmission electron microscopy (TEM). Briefly, holey carbon grids for electron microscopy (Quantifoil 2×1, Electron Microscopy Sciences, Hatfield, Pa) were hydrophilized for 25 seconds. Five microliters of EV suspension was deposited on the grids and incubated for 1 minute. The grid was mounted on a semiautomatic Cryoplunge-Gatan CP3 (Gatan, Pleasanton, Calif) and plunged in liquid ethane cooled with liquid nitrogen to preserve

the fully hydrated structures in amorphous ice. The grids were then transferred under liquid nitrogen into a FEI Tecnai Arctica TEM (FEI, Hillsboro, Ore) operated at 200 kV equipped with a field emission gun and autoloader (Thermo Fisher). Digital images were collected at low-dose conditions (~24 e-/A2 s) at 23,500× and 39,000× magnification with a charge-coupled device camera at 3.83 and 2.5 A per pixel resolution, respectively.

EV labeling and cellular uptake

EV membranes were labeled with a fluorescent dye using an ExoGlow-membrane EV labeling kit (System Biosciences) for intracellular tracking and visualization. Briefly, EVs were mixed with the reaction buffer containing labeling dye and incubated for 30 minutes at room temperature. To remove free unlabeled dye, ExoQuick-TC was added to the EV sample, incubated for 30 minutes at 4°C, and centrifuged for 10 minutes at 10,000 rpm at 4°C. The resulting labeled EVs were resuspended in BEBM, added to the cells, and incubated for 10, 30, or 60 minutes at 37°C. To further investigate the endocytic mechanism, cells were pretreated with a clathrin-mediated endocytosis inhibitor (chlorpromazine, 25 μmol) for 30 minutes before the addition of EVs. Low-temperature incubation at 4°C was also carried out. After incubation with EVs, cells were washed with PBS, fixed with 4% paraformaldehyde (Thermo Fisher), and stained with 4′,6-diamidino-2-phenylindole (DAPI, 1 μg/mL; Thermo Fisher). The stained cells were observed with a Zeiss LSM 800 confocal microscope (Carl Zeiss, Jena, Germany) with a 20× objective.

Determination of virus-induced cytopathic effect

HNEpCs were incubated with betacoronavirus 1 (CoV_OC43, strain designation OC43; American Type Culture Collection [ATCC], Manassas, Va), rhinovirus 1B (RV-1B, strain designation B632; ATCC), and rhinovirus 16 (RV-16, strain designation 11757; ATCC) in BEBM at half-log serial dilutions. After 1 hour of virus absorption, BEGM was added to the experimental wells, and the incubation was continued. Four days after infection, morphologic changes in the virus-infected cells were observed under a bright-field microscope (BZ-X710, Keyence, Osaka, Japan) with a 20× objective. Virus tissue culture infective dose was then quantified via a Viral ToxGloassay (Promega). Briefly, ATP detection reagent was added to the cells and incubated for 10 minutes before measuring luminescence with a microplate reader (Synergy H1). Median tissue culture infective dose ($TCID_{50}$) values were calculated by plotting net relative luminescence unit values after subtracting the average of blank wells against viral dilution.

Immunofluorescence staining

HNEpCs were incubated with viruses in BEBM. After 1 hour of virus absorption, BEGM was added to the experimental wells, and the incubation was continued. Four days after infection, cells were washed with PBS, fixed with 4% paraformaldehyde, and blocked with PBS containing 2% bovine serum albumin (BSA), 5% goat serum, and 0.2% Triton X-100 for 1 hour at room temperature. Subsequently, cells were incubated with the anti-dsRNA antibody (clone rJ2 antibody; Sigma-Aldrich) diluted at 1:60 in the same blocking buffer overnight at 4°C and the Alexa Fluor 488–conjugated goat anti-mouse IgG secondary antibody (1:2000 dilution; Thermo Fisher) for 1 hour at room temperature. Nuclei were counterstained with DAPI at a concentration of 1 μg/mL, which was premixed with the secondary antibody in PBS. The stained cells were photographed using a charge-coupled device camera–installed fluorescence microscope (BZ-X710, Keyence) with a 20× objective.

Antiviral activity assay

Viruses at 2 times the $TCID_{50}$ were premixed with recombinant human low-density lipoprotein receptor (LDLR; 60 nmol; R&D Systems, Minneapolis, Minn), recombinant human intercellular adhesion molecule 1 (ICAM-1; 60 nmol; R&D Systems), or purified EVs at a concentration of 1.25×10^{10}/mL in BEBM at a volume ratio of 1:1 and incubated for 1 hour. HNEpCs seeded in a 96-well plate were then exposed to viruses, which were preincubated with recombinant human proteins or EVs. After 1 hour of virus absorption, BEGM was added to the experimental wells and the incubation was continued. Four days after infection, virus RNA was extracted from the infected cells and the expression quantified by real-time quantitative PCR (qPCR).

RNA interference transfection in HNEpCs

Dose–response transfection experiments were performed on HNEpCs grown to 80% confluence in 12-well plates. Increasing doses of small interfering RNAs (siRNAs)/miRNA mimics/miRNA inhibitors (0.1, 1, 10, and 100 nmol; Thermo Fisher) were mixed with Lipofectamine 2000 in BEBM and incubated at room temperature for 15 minutes. The complex was then added to the cells in BEGM; the culture was continued for 48 hours and 72 hours for transfection of miRNA mimic/inhibitor and siRNA, respectively. Nontargeting siRNA (siNC), random sequence miRNA mimic (miRNA mimic negative control), and random sequence miRNA inhibitor (anti–miR-NC) were used as negative controls. The efficiency of transfection for targeting miR-17, LDLR, and ICAM-1 was validated by qPCR. HNEpCs used for EV production were grown in T-75 flasks. After transfection with the 30 nmol siRNA/miRNA mimic/miRNA inhibitor dose for predetermined time periods (24 hours and 48 hours for miRNA mimic/inhibitor and siRNA transfection, respectively), the *in vitro* poly(I:C) stimulation was performed as described above. The secreted EVs in media were isolated, validated, and used for downstream applications.

RNA extraction, complementary DNA synthesis, and qPCR

Total RNA was isolated from EVs using a total exosome RNA and protein isolation kit (Thermo Fisher) in accordance with the manufacturer's protocol. Total RNA was extracted from cells using TRIzol reagent, *mir*Vana miRNA isolation kit, or TaqMan fast advanced cells-to-ct kit (Thermo Fisher) in accordance with the manufacturer's protocol. The extracted RNA was treated with RNase-free DNase I to remove contaminating genomic DNA and reverse transcribed to complementary DNA template using the thermal cycler (Bio-Rad, Hercules, Calif). For complementary DNA synthesis from miRNA, TaqMan advanced miRNA assays (Thermo Fisher) were used. Subsequently, qPCR was performed in the Roche Light Cycler 480 PCR system (Roche, Basel, Switzerland) with TaqMan gene expression master mix. Gene-specific primers for human 18S ribosomal RNA (Hs99999902_s1), ICAM-1 (Hs00164932_m1), LDLR (Hs00181192_m1), IFN-α (Hs00265051_s1), IFN-β (Hs01077958_s1), U6 small nuclear RNA (TM: 001973), miR-17 (478447_mir), and CoV_OC43 (Vi0639646_s1) were used to detect the expression. Human rhinovirus gene expression was detected via the Genesig advanced kit (Primerdesign, London, England, United Kingdom). The $2^{-\Delta\Delta Ct}$ method was used to analyze the relative changes of gene expression after normalization to the expression of internal control.

miRNA profiling

The NanoString nCounter platform (NanoString Technologies, Seattle, Wash) was used to evaluate miRNA expression with the nCounter human v3 miRNA panel (NanoString Technologies). The panel includes unique tags for 799 miRBase high-confidence annotated human miRNAs and 5 housekeeping genes for normalization of expression between samples. Each sample was analyzed by using 100 ng of total RNA isolated from EVs for processing and overnight hybridization at 65°C to the probe pairs, consisting of a reporter probe, which carries the signal on its 5′ end, and a capture probe, which holds biotin on its 3′ end. After hybridization, sample cleanup and counting were carried out in accordance with the manufacturer's protocol. Count normalization and miRNA expression analysis were performed by nSolver 4.0 software (NanoString Technologies).

Protein extraction

Intracellular proteins were extracted using a Pierce radioimmunoprecipitation assay buffer (Thermo Fisher). Proteins in EVs were isolated using the total exosome RNA and protein isolation kit (Thermo Fisher). Protein concentrations were determined by a Pierce BCA protein assay kit.

Western blot and ELISA

Proteins were separated by sodium dodecyl sulfate–polyacrylamide gel electrophoresis and transferred to a polyvinylidene fluoride membrane (Thermo Fisher). The membrane was then blocked with a StaringBlock T20 (Tris-buffered saline) blocking buffer (Thermo Fisher) for 1 hour at room temperature and incubated with primary antibodies in the blocking buffer overnight at 4°C as well as secondary antibodies for 1 hour at room temperature. Primary antibodies, including TLR3 (1:1000 dilution, #6961, Cell Signaling Technology, Danvers, Mass), phospho-IRF3 (1:1000 dilution, #4947, Cell Signaling Technology), IRF3 (1:1000 dilution, #11904, Cell Signaling Technology), and GAPDH (1:1000 dilution, #2118, Cell Signaling Technology), were used. A goat anti-rabbit IgG horseradish peroxidase–conjugated secondary antibody (1:10,000 dilution, Thermo Fisher) was also used. Pierce ECL Western blot substrate (Thermo Fisher) was used for enhanced chemiluminescence detection of blots, and signals were detected with a ChemiDoc MP imaging system (Bio-Rad). Quantikine ELISA kits for ICAM-1 and LDLR (R&D Systems) were used to determine the expression of intracellular and EV proteins in accordance with the manufacturer's protocol. All values were normalized to total protein concentration within the same sample.

Immunogold TEM of EVs and viruses

The immunogold TEM procedure was adapted from Théry et al.[34] Purified EVs were premixed with RV-1B or RV-1B, incubated for 1 hour at 37°C, and fixed for 30 minutes at room temperature in 2% paraformaldehyde in 0.1 mol sodium phosphate buffer (Electron Microscopy Sciences). Five microliters of sample was absorbed onto formvar/carbon-coated electron microscopy grids (Electron Microscopy Sciences) for 20 minutes. After absorption, the grids were rinsed in PBS twice and then transferred to PBS/50 mmol glycine (Sigma-Aldrich) for 4 washes. Grids were blocked in 5% BSA (Thermo Fisher) in PBS for 10 minutes at room temperature. The grids were incubated at 4°C overnight in the primary antibody cocktail (1:10 dilution, anti-CD81 antibody produced in rabbit; Sigma-Aldrich; 1:5, rhinovirus VP3 monoclonal antibody; Thermo Fisher) diluted in 1% BSA in PBS. The grids were then rinsed in 0.1% BSA in PBS 6 times. The secondary antibody cocktail (1:20 dilution, goat–anti-rabbit IgG H&L, EM-grade 15 nm; 1:20 dilution, goat–anti-mouse IgG H&L, EM-grade 10 nm; Electron Microscopy Sciences) in 1% BSA in PBS was then applied for 1 hour at room temperature and rinsed 6 times with 0.5% BSA in PBS followed by 8 times with PBS. The grids were incubated in 1% glutaraldehyde in 0.1 mol sodium phosphate buffer for 5 minutes. After rinsing 8 times in deionized water, grids were contrasted in uranyl acetate–oxalate solution and uranyl-methyl cellulose (Electron Microscopy Sciences) for 5 minutes each. The grids were blotted on filter paper and air-dried before imaging. The EVs and viruses were observed with an FEI Tecnai G2 Spirit transmission electron microscope at an accelerating voltage of 100 kV interfaced with an AMT XR41 digital CCD camera (Advanced Microscopy Techniques, Woburn, Mass) for digital TIFF file image acquisition. Purified mouse IgG_1 κ isotype control and purified rabbit IgG isotype standard (BD Biosciences, San Jose, Calif) were used as negative controls.

Statistical analysis

At least 3 independent experiments were performed. Data points were expressed as mean values plus or minus standard errors of the mean (means ± SEMs). To determine statistical significance, Student *t* test or analysis of variance (1-way or 2-way ANOVA) followed by Tukey multiple comparison test was performed by GraphPad Prism 8 software (GraphPad Software, La Jolla, Calif). Differences were considered statistically significant if $P \leq .05$.

RESULTS

TLR3 stimulation induces nasal epithelial EV secretion

The first experiment was designed to determine whether nasal epithelial EV secretion was influenced by TLR3 stimulation. Validation of EV isolation and purification procedures was performed as described in the Methods in this article's Online Repository (available at www.jacionline.org). We confirmed that purified EVs displayed EV-enriched marker CD81 and lacked expression of endoplasmic reticulum protein markers calnexin and GRP94 as well as Golgi marker GM130 (see Fig E1 in the Online Repository). Poly(I:C) was used to activate the TLR3 signaling pathway, as it is a canonical TLR3 agonist and has been commonly used to mimic the response to RNA viral infections.[35] Using primary HNEpCs, we demonstrated that poly(I:C) was capable of stimulating nasal epithelial EV secretion in both time- and dose-dependent manners (Fig 1, *A*). We found that poly(I:C) began promoting EV secretion at 5 hours after stimulation, with a peak release effect observed at 24 hours. The 2.5 μg/mL dose exhibited the most significant induction, with a peak effect of approximately 1.6-fold at 24 hours relative to vehicle controls ($P \leq .005$) without inducing cytotoxicity, as determined by MTS assay (Fig 1, *B*).

After confirmation that poly(I:C) exposure induced an increase in nasal epithelial EV secretion, we next validated that this effect was mediated by activating the TLR3-IRF3 signaling axis. In the presence of poly(I:C), pretreating the cells with a TLR3/dsRNA complex inhibitor downregulated the protein expression of TLR3 and phospho-IRF3 (Fig 1, *C* and *D*) and negatively affected the poly(I:C)-stimulated effect on EV secretion (Fig 1, *E*). The total number of secreted EVs was comparable to that of unstimulated controls ($P > .05$). However, when cells were pretreated with the cocktail of TLR3/dsRNA complex inhibitor and IRF3 agonist KIN1148, the blocking of the TLR3-IRF3 signaling axis and reduction in EV secretion induced by the competitive binding to TLR3 were completely abrogated (Fig 1, *C-E*).

Having confirmed that poly(I:C) stimulated the secretion of nasal epithelial EVs through the TLR3 signaling pathway, we next characterized TLR3-stimulated EVs compared to unstimulated control EVs. TLR3-stimulated EVs exhibited an average particle size of 177.5 ± 20.1 nm and a negative surface charge with zeta potential of −10.88 ± 1.31 mV (Table I). Using cryogenic TEM, we confirmed that TLR3-stimulated EVs appeared as single or double membranous vesicles with the expected size of approximately 100 nm (Fig 1, *F*).[34] Finally, we explored the interepithelial transport kinetics of TLR3-stimulated EVs to primary autologous HNEpCs. After fluorescent labeling, TLR3-stimulated EVs were exposed to cultured HNEpCs over 60 minutes at 37°C. As shown in Fig 1, *G,* the EV-derived fluorescent tag was detected intracellularly within 10 minutes, indicating rapid cellular uptake, which then progressively diffused throughout the cytoplasm over 60 minutes. Furthermore, we found that EV uptake was significantly suppressed by 87.5% ($P \leq .001$) and 41.3% ($P \leq .01$) when cells were incubated at a low temperature of 4°C and pretreated with chlorpromazine, respectively, confirming that energy-dependent and clathrin-mediated endocytosis was involved in EV internalization in HNEpCs (Fig 1, *H*). Of note, the properties of TLR3-stimulated EVs were not significantly distinct from those of unstimulated control EVs (see Fig E2 in the Online Repository at www.jacionline.org).

TLR3-stimulated EVs exhibit potent antiviral activity against respiratory viruses

Having confirmed that TLR3 stimulation significantly increased nasal epithelial EV secretion, we next studied whether

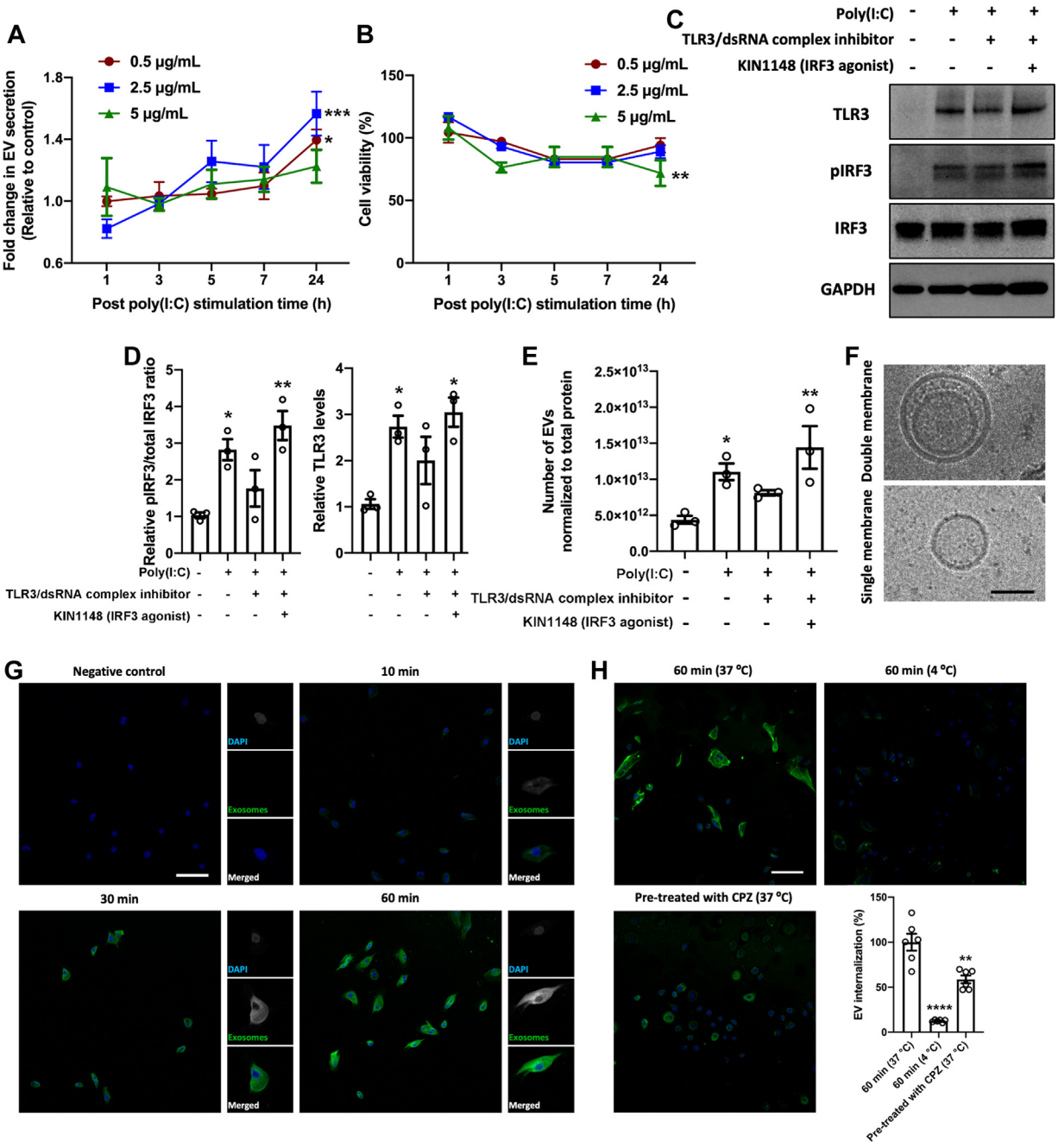

FIG 1. TLR3 stimulation induces nasal epithelial EV secretion. **(A)** Dose and time responses in numbers of EVs secreted from HNEpCs stimulated with a TLR3 agonist poly(I:C). ***$P \leq .005$ and *$P \leq .05$ (2-way ANOVA followed by Tukey test); data represent 4 independent experiments (means ± SEMs). **(B)** Cell viability of HNEpCs after TLR3 stimulation. **$P \leq .01$ (2-way ANOVA followed by Tukey test); data represent 4 independent experiments (means ± SEMs). **(C)** Western blot analysis of TLR3 and phospho-IRF3 protein expression in poly(I:C) stimulated HNEpCs with or without pretreatment of TLR3/dsRNA complex inhibitor (10 μmol) and IRF3 agonist (KIN1148, 10 μmol). **(D)** Quantification of protein expression of phospho-IRF3 normalized to total IRF controls and TLR3 normalized to GAPDH controls by densitometry analysis. **$P \leq .01$ and *$P \leq .05$ (1-way ANOVA followed by Tukey test); data represent 3 independent experiments (means ± SEMs). **(E)** Numbers of EVs secreted from poly(I:C)-stimulated HNEpCs with or without TLR3 signaling pathway interrogation. **$P \leq .01$ and *$P \leq .05$ (1-way ANOVA followed by Tukey test); data represent 3 independent experiments (means ± SEMs). **(F)** Representative cryogenic electron microscopic images of TLR3-stimulated EVs; scale bar = 50 nm. **(G)** Representative confocal microscopic images of fluorescent dye–labeled TLR3-stimulated EV uptake in HNEpCs over 60 minutes; scale bar = 100 μm. **(H)** Representative confocal microscopic images of fluorescent dye–labeled, TLR3-stimulated EV uptake in HNEpCs for 60 minutes in different conditions (37°C vs 4°C and with or without pretreatment of clathrin-mediated endocytosis inhibitor (chlorpromazine [CPZ], 25 μmol) and quantitative analysis of corrected fluorescence integrated density indicating percentage of EV internalization in HNEpCs; scale bar = 100 μm. ****$P \leq .001$ and **$P \leq .01$ (1-way ANOVA followed by Tukey test); data represent 6 independent experiments (means ± SEMs).

TABLE I. Particle size and zeta potential of EVs secreted from HNEpCs

EV	Particle size (d·nm)	Zeta potential (mV)
Control	179.8 ± 5.5	−15.35 ± 0.49
TLR3 stimulated	177.5 ± 20.1	−10.88 ± 1.31

these EVs displayed intrinsic antiviral activity. We first established an infection model in primary HNEpCs with 3 different common respiratory viruses, including coronavirus CoV_OC43, minor group rhinovirus RV-1B, and major group rhinovirus RV-16, as model upper respiratory tract pathogens. We validated the viral infectivity in host cells by determining $TCID_{50}$ of 3 types of viruses. As shown in Fig 2, *A,* all 3 types of viruses produced cytopathic effects in primary HNEpCs in a dose-dependent manner; the $TCID_{50}$ values were 55-, 4778-, and 591-fold dilution for CoV_OC43, RV-1B, and RV-16, respectively. Virus-induced cytopathic effects were also further confirmed by changes in host cell morphology, including vacuolization of cytoplasm, rounding, and sloughing (Fig 2, *B*). To validate the production of dsRNA in viral infections, we performed immunofluorescence staining on primary HNEpCs exposed to viruses at their $TCID_{50}$. No fluorescence signal was observed in uninfected control cells, whereas perinuclear pattern of dsRNA staining was detected in infected cells at 96 hours after virus exposure (Fig 2, *B*). Intracellular mRNA levels of IFN-α and IFN-β at 96 hours after infection were consistently and significantly higher than those of uninfected controls, indicating successful induction of cytopathic effects and host cell immune responses (Fig 2, *C,* $P \leq .05$).

After validation of the infection model in primary HNEpCs, we next evaluated the *in vitro* antiviral activity mediated by TLR3-stimulated EVs using the culture model. We found that exposure to TLR3-stimulated EVs resulted in a significant reduction in intracellular virus mRNA levels relative to untreated cells infected with the same virus titer, indicating suppressed virus replication (Fig 2, *D,* $P \leq .001$). Moreover, TLR3-stimulated EVs blocked viral infection in a dose-dependent manner and resulted in 38.37%, 72.59%, and 61.51% inhibition of the replication of CoV_OC43 ($P \leq .05$), RV-1B ($P \leq .001$), and RV-16 ($P \leq .001$), respectively, even at the lowest concentration of 2.5×10^9/mL (Fig 2, *D*). In contrast, unstimulated control EVs had negligible effects on suppression of viral infection. No significant difference in virus mRNA level was observed between untreated infected cells and those treated with unstimulated control EVs, suggesting that TLR3 stimulation may alter cargo in EVs and confer enhanced antiviral properties to EVs (Fig 2, *E,* $P > .05$).

TLR3 stimulation upregulates miR-17 in EVs, which confers enhanced antiviral activity

Having demonstrated that TLR3-stimulated EVs exhibited antiviral activity against multiple common respiratory viruses, we next explored the potential antiviral mechanisms with a focus on the role of miRNAs. We sought to profile the miRNA expression changes in EVs using NanoString to understand the correlation between differentially expressed miRNAs and antiviral effects of TLR3-stimulated EVs. Fig 3, *A,* shows distinct expression patterns with 594 miRNAs upregulated in TLR3-stimulated EVs compared to control EVs. Hierarchical cluster analysis reveals that miRNA expression levels of individual TLR3-stimulated EV samples were well correlated with each other and different from control EV samples. This is represented by the common nodes joining the samples, which have closest distance according to miRNA expression. After confirmation of differential miRNA profiles of EVs with and without TLR3 stimulation, data were analyzed by volcano plot, and 6 miRNAs that are significantly upregulated after TLR3 stimulation and are associated with antiviral roles were highlighted (Fig 3, *B*). Among these miRNAs, miR-17 has previously been reported to suppress virus replication during URIs,[36,37] so it was therefore selected for further validation as a mechanism-of-action target.

Using qPCR, we again verified that TLR3 stimulation significantly increased the expression of miR-17 in EVs compared to the unstimulated control (Fig 3, *C,* $P \leq .001$). Transfection of synthetic miR-17 mimic into primary HNEpCs efficiently upregulated the expression of miR-17 in a dose-dependent manner (see Fig E3, *A,* in the Online Repository at www.jacionline.org). The highest concentration of 100 nmol was chosen and was used in the subsequent antiviral experiments as a result of its significance relative to vehicle control ($P \leq .05$). We found that transfection of miR-17 mimic suppressed virus RNA replication with significantly reduced intracellular virus mRNA levels of CoV_OC43 ($P \leq .01$), RV-1B ($P \leq .05$), and RV-16 ($P \leq .05$) in host cells, confirming the robust antiviral activity of miR-17 against respiratory viruses (Fig 3, *D*). As a secondary validation, we used a mirVana miR-17 inhibitor to achieve specific knockdown of miR-17 in TLR3-stimulated EVs. Transfection of miR-17 inhibitor into donor HNEpCs significantly downregulated the expression of miR-17 in a dose-dependent manner (Fig E3, *B*). Because the highest dose of 100 nmol exhibited over 99% efficacy in inhibiting miR-17 expression without causing cytotoxicity, it was used to produce TLR3-stimulated miR-17 knockdown EVs (anti–miR-17 EVs). Fig 3, *E,* confirms that transfection of miR-17 inhibitor at 100 nmol significantly downregulated the expression of miR-17 in TLR3-stimulated EVs, as quantified by using qPCR ($P \leq .001$). Remarkably, intracellular virus mRNA levels of CoV_OC43 ($P \leq .05$), RV-1B ($P \leq .05$), and RV-16 ($P \leq .05$) in recipient infected cells after exposure to anti–miR-17 EVs were significantly higher than those treated with TLR3-stimulated nontargeting negative control EVs (anti–miR-NC EVs), indicating that the abundance of miR-17 in EVs induced by TLR3 stimulation confers enhanced antiviral activity (Fig 3, *F*).

TLR3-stimulated EV surface receptor–virus interactions contribute to antiviral activity and prevent virus entry into host cells

Because EVs have been previously shown to inhibit infections by blocking the virus protein binding with its cellular receptor in host cells,[32] we analyzed the levels of LDLR, ICAM-1, and *N*-acetylneuraminic acid (NANA), which are involved in receptor-mediated endocytosis of RV-1B, RV-16, and CoV_OC43, respectively. We found that TLR3 stimulation significantly upregulated LDLR in EVs at both the transcriptional (Fig 4, *A,* $P \leq .005$) and translational (Fig 4, *B,* $P \leq .001$) level compared to unstimulated controls, suggesting that TLR3 stimulation promotes the packaging of surface receptor proteins within EVs. Similarly, TLR3 stimulation induced an abundance of

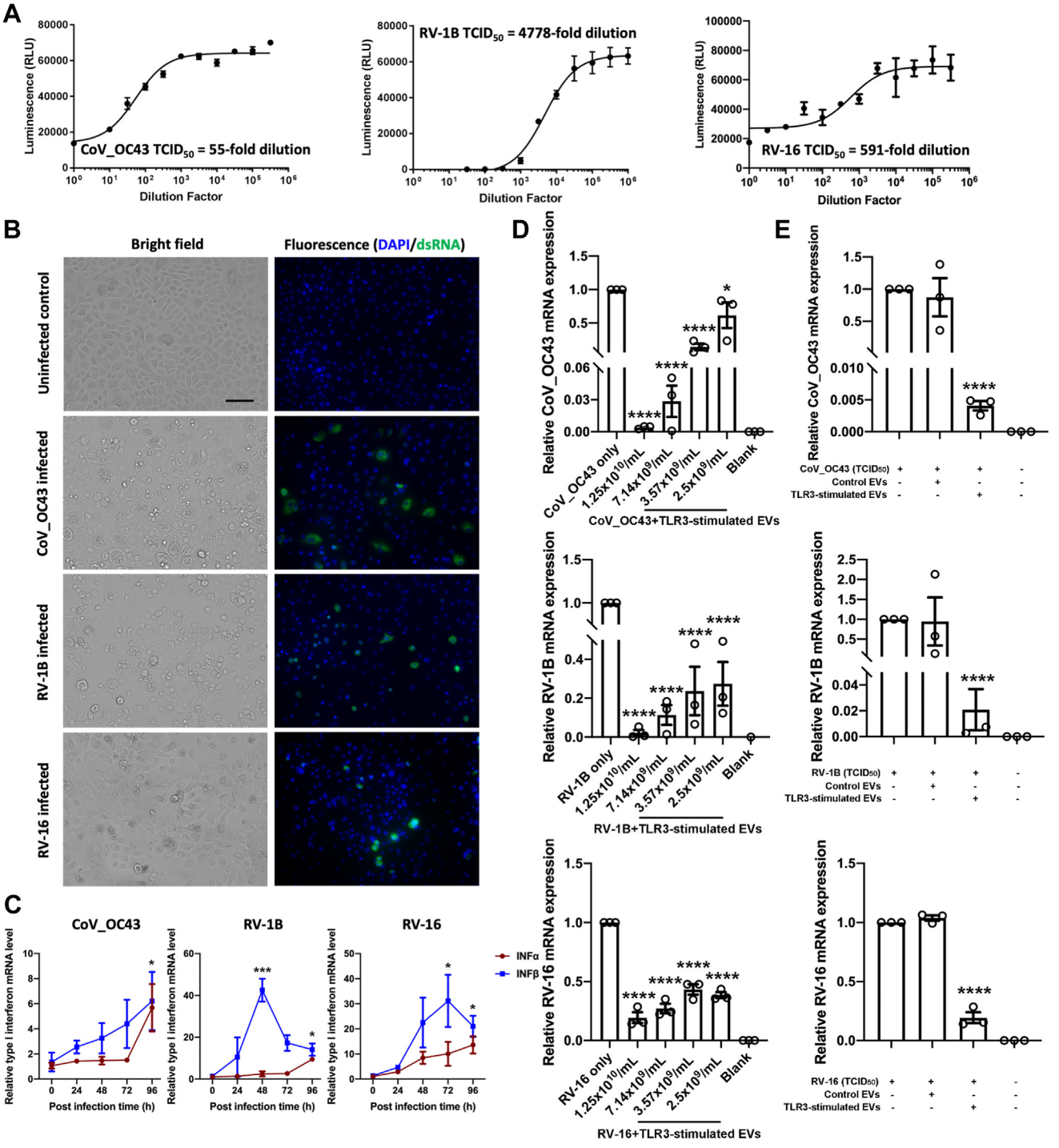

FIG 2. TLR3-stimulated EVs exhibit potent antiviral activity against respiratory viruses. **(A)** Viral ToxGlo assay determining $TCID_{50}$ of coronavirus CoV_OC43, minor group rhinovirus RV-1B, and major group rhinovirus RV-16 in HNEpCs; data represent 3 independent experiments (means ± SEMs). **(B)** Representative bright-field and fluorescent microscopic images of HNEpCs infected with CoV_OC43, RV-1B, or RV-16 (virus-infected cells stained with double-strand RNA antibody and DAPI); scale bar = 100 μm. **(C)** qPCR analysis showing mRNA levels of type I interferons in virus-infected HNEpCs at different time points after infection. $^{*}P \leq .05$ and $^{***}P \leq .005$ (1-way ANOVA followed by Tukey test); data represent 3 independent experiments (means ± SEMs). **(D)** qPCR analysis showing virus mRNA levels in HNEpCs infected by viruses ($TCID_{50}$) after preincubation with TLR3-stimulated EVs at different concentrations (2.5×10^9/mL to 1.25×10^{10}/mL). $^{*}P \leq .05$ and $^{****}P \leq .001$ (1-way ANOVA followed by Tukey test); data represent 3 independent experiments (means ± SEMs). **(E)** qPCR analysis showing virus mRNA levels in HNEpCs infected by viruses after preincubation with control or TLR3-stimulated EVs at the concentration of 1.25×10^{10}/mL. $^{****}P \leq .001$ (1-way ANOVA followed by Tukey test); data represent 3 independent experiments (means ± SEMs).

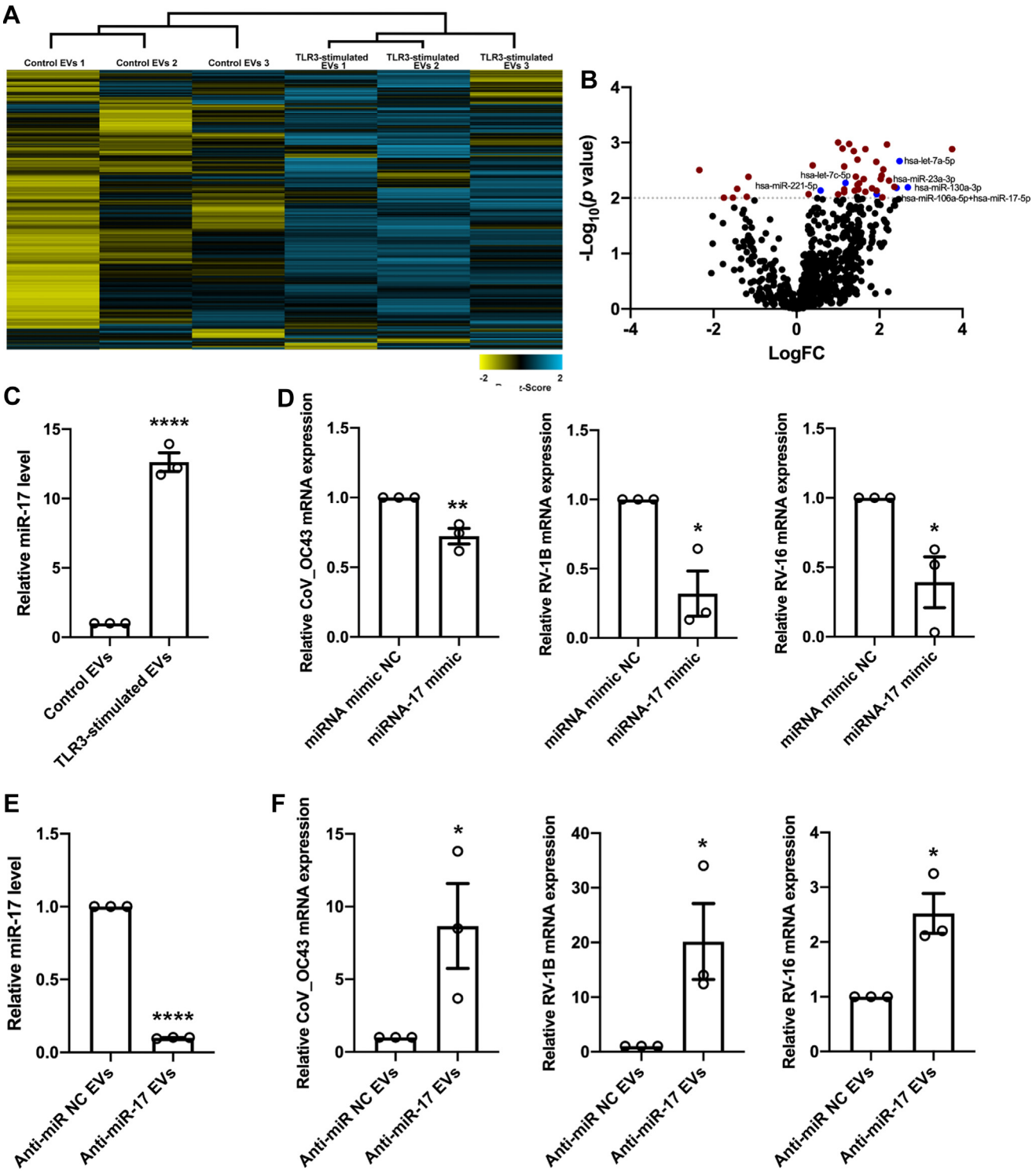

FIG 3. TLR3 stimulation upregulates miR-17 in EVs, which confers enhanced antiviral activity. **(A)** Heat map showing clustering of control and TLR3-stimulated EVs according to different miRNA expression patterns. **(B)** Volcano plot of differentially expressed miRNAs in control and TLR3-stimulated EVs. Significantly changed miRNAs after TLR3 stimulation were defined as $P \leq .01$. **(C)** qPCR analysis showing increased miR-17 expression in EVs after TLR3 stimulation. $^{****}P \leq .001$ (2-tailed Student *t* test). **(D)** qPCR analysis showing reduced virus mRNA levels in HNEpCs infected with CoV_OC43, RV-1B, or RV-16 when transfected with miR-17 mimic compared to miRNA mimic negative control. $^{**}P \leq .01$ and $^{*}P \leq .05$ (2-tailed Student *t* test). **(E)** qPCR analysis showing miR-17 levels in TLR3-stimulated EVs with (anti–miR-17) or without (anti–miR-NC) knockdown of miR-17. $^{****}P \leq .001$ (2-tailed Student *t* test). **(F)** qPCR analysis showing increased virus mRNA levels in HNEpCs infected by CoV_OC43, RV-1B, or RV-16 when preincubated viruses with TLR3-stimulated anti–miR-17 EVs compared to TLR3-stimulated anti–miR-negative control EVs. $^{*}P \leq .05$ (2-tailed Student *t* test); data represent 3 independent experiments (means ± SEMs).

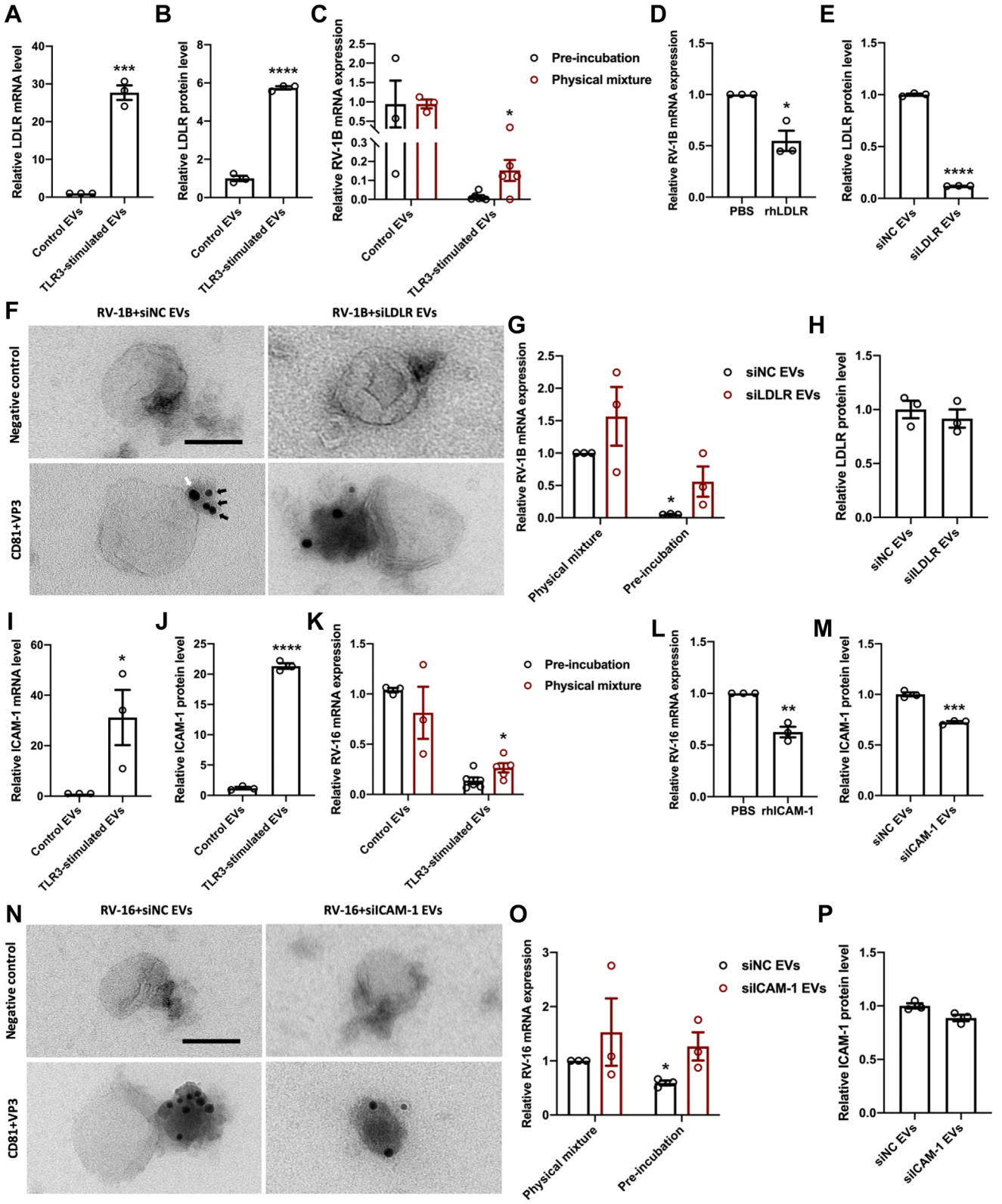

FIG 4. TLR3-stimulated EV surface receptor–virus interactions contribute to antiviral activity and prevent virus entry into host cells. (**A** and **B**) qPCR and ELISA analysis showing increased LDLR mRNA *(A)* and protein *(B)* levels in EVs after TLR3 stimulation. ****$P \leq .001$ and ***$P \leq .005$ (2-tailed Student *t* test). **(C)** qPCR analysis showing reduced virus mRNA levels in HNEpCs infected by RV-1B after preincubation with TLR3-stimulated EVs relative to control EVs and coincubation (physical mixture). *$P \leq .05$ for comparison between physical mixture and preincubation (2-way ANOVA followed by Tukey test). **(D)** qPCR analysis showing reduced virus

ICAM-1 mRNA (Fig 4, *I*, $P \leq .05$) and protein (Fig 4, *J*, $P \leq .001$) in EVs. NANA was undetectable in both unstimulated control and TLR3-stimulated EVs for technical reasons; however, the amount of intracellular NANA was significantly increased on TLR3 stimulation (see Fig E4 in the Online Repository at www.jacionline.org; $P \leq .001$).

After determining that TLR3 stimulation upregulated LDLR and ICAM-1 in EVs, we next studied whether the enrichment in surface receptor proteins was associated with intrinsic antiviral activity mediated by TLR3-dependent EVs. We found TLR3-stimulated EVs exhibited more robust antiviral effects against RV-1B (Fig 4, *C*, $P \leq .05$) and RV-16 (Fig 4, *K*, $P \leq .05$) when they were preincubated with viruses for 1 hour at 37°C before exposure to recipient host cells relative to coincubation (physical mixture of EVs and viruses). This suggests that TLR3-stimulated EV surface receptor protein–virus interactions could suppress viral infections by functioning as decoys, thereby preventing virus from binding with its cellular receptor in human host cells. In contrast, unstimulated control EVs showed no significant effect on blocking viral infections, regardless of whether EVs were preincubated with virus es (Fig 4, *C* and *K*, $P > .05$).

RV-1B and RV-16 primarily utilize LDLR and ICAM-1 as their initial tethering receptors, respectively, for cell entry. We demonstrated that RV-1B and RV-16 infection in primary HNEpCs could therefore be blocked by soluble recombinant human protein recombinant human LDLR (Fig 4, *D*, $P \leq .05$) and recombinant human ICAM-1 (Fig 4, *L*, $P \leq .01$), respectively. To explore the role of LDLR and ICAM-1 in EVs in suppression of viral infections, we used siRNAs targeting the LDLR or ICAM-1 mRNA sequences to specifically silence gene expression in TLR3-stimulated EVs. The gene-silencing efficiency of siRNAs was confirmed by qPCR. The transfection of LDLR or ICAM-1 siRNA into primary HNEpCs showed efficient silencing of the target mRNA level in a dose-dependent manner (Fig E3, *C* and *D*). Because of the moderate cytotoxicity we observed at the highest concentration of 100 nmol, the final concentration of 30 nmol was selected and used in the next experiment to produce gene-knockdown EVs. As shown in Fig 4, *E* and *M*, both LDLR ($P \leq .001$) and ICAM-1 ($P \leq .005$) siRNAs significantly downregulated target proteins in TLR3-stimulated EVs, as quantified by LDLR and ICAM-1 ELISA assays.

After validation of gene-knockdown EVs, we evaluated the mechanism of surface receptor proteins in neutralizing virus binding with its cellular receptor and mediating the antiviral activity of TLR3-stimulated EVs. Using immunogold labeling and TEM, we found that 10 nm nanogold particles labeling rhinovirus surface protein VP3 largely localized to the membrane of TLR3-stimulated negative control (siNC) EVs, where 15 nm nanogold particles labeling CD81 presented (Fig 4, *F*). The number of 10 nm nanogold particles, which labeled RV-1B and bound to CD81 positively stained TLR3-stimulated LDLR-silencing (siLDLR) EVs, significantly decreased compared to that of TLR3-stimulated siNC EVs (Fig 4, *F*, and see Fig E5, *A*, in the Online Repository at www.jacionline.org; $P \leq .01$). These observations confirmed that robust binding between RV-1B and TLR3-stimulated EVs occurred after preincubation and was associated with LDLR in EVs. In addition, we found that intracellular virus mRNA level of RV-1B was significantly increased when host cells were exposed to RV-1B, which was preincubated with TLR3-stimulated siLDLR EVs relative to TLR3-stimulated siNC EVs (Fig 4, *G*, $P \leq .05$). This suggested that knockdown of LDLR in EVs weakens the interaction between RV-1B and TLR3-stimulated EVs, thereby facilitating virus entry into host cells. No significant difference in virus mRNA level was observed between TLR3-stimulated siLDLR EVs and control counterparts in the absence of preincubation (Fig 4, *G*, $P > .05$). Additionally, the LDLR protein level in recipient cells was not significantly altered on administration of siLDLR EVs compared to siNC EVs, suggesting that the blocking effect of EVs was principally dependent on their binding affinity with viruses rather than their modulation of receptor levels on target cells (Fig 4, *H*, $P > .05$). Similar results were detected regarding the effect of ICAM-1 knockdown on TLR3-stimulated EV surface receptor–virus interactions and consequent antiviral activity against RV-16 (Fig 4, *N-P*, and Fig E5, *B*).

mRNA levels in HNEpCs infected by RV-1B, which were preincubated with recombinant human LDLR (rhLDLR) relative to PBS. $*P \leq .05$ (2-tailed Student *t* test). **(E)** ELISA analysis confirming reduced LDLR protein levels in TLR3-stimulated EVs when transfected with LDLR siRNA (siLDLR) compared to negative control (siNC). $****P \leq .001$ (2-tailed Student *t* test). **(F)** TEM images demonstrating the binding between RV-1B and siLDLR or siNC EVs with immunogold labeling of rhinovirus marker VP3 (10 nm nanogold particles) and EV marker CD81 (15 nm nanogold particles) localizing to the EV membrane; *white arrows* indicate 15 nm nanogold particles; *black arrows,* 10 nm nanogold particles; scale bar = 100 nm. **(G)** qPCR analysis showing abrogation of antiviral activity in HNEpCs infected by RV-1B after preincubation with TLR3-stimulated siLDLR EVs relative to siNC EVs. $*P \leq .05$ for comparison between physical mixture and preincubation (2-way ANOVA followed by Tukey test). **(H)** ELISA analysis showing intracellular LDLR protein levels in recipient cells after incubation with siLDLR or siNC EVs. (**I** and **J**) qPCR and ELISA analysis showing increased ICAM-1 mRNA *(I)* and protein *(J)* levels in EVs after TLR3 stimulation, respectively. $****P \leq .001$ and $*P \leq .05$ (2-tailed Student *t* test). **(K)** qPCR analysis showing reduced virus mRNA levels in HNEpCs infected by RV-16 after preincubation with TLR3-stimulated EVs relative to control EVs and coincubation (physical mixture). $*P \leq .05$ for comparison between physical mixture and preincubation (2-way ANOVA followed by Tukey test). **(L)** qPCR analysis showing reduced virus mRNA levels in HNEpCs infected by RV-16, which were preincubated with rhICAM-1 relative to PBS. $**P \leq .01$ (2-tailed Student *t* test). **(M)** ELISA analysis confirming reduced ICAM-1 protein levels in TLR3-stimulated EVs when transfected with ICAM-1 siRNA (siICAM-1) compared to siNC. $***P \leq .005$ (2-tailed Student *t* test). **(N)** TEM images demonstrating the binding between RV-16 and siICAM-1 or siNC EVs with immunogold labeling of VP3 and CD81; scale bar = 100 nm. **(O)** qPCR analysis showing abrogation of antiviral activity in HNEpCs infected by RV-16 after preincubation with TLR3-stimulated siICAM-1 EVs relative to siNC EVs. $*P \leq .05$ for comparison between physical mixture and preincubation (2-way ANOVA followed by Tukey test). **(P)** ELISA analysis showing intracellular ICAM-1 protein levels in recipient cells after incubation with siICAM-1 or siNC EVs. Data shown in this figure represent at least 3 independent experiments (means ± SEMs). *rh,* Recombinant human; *si,* small interfering.

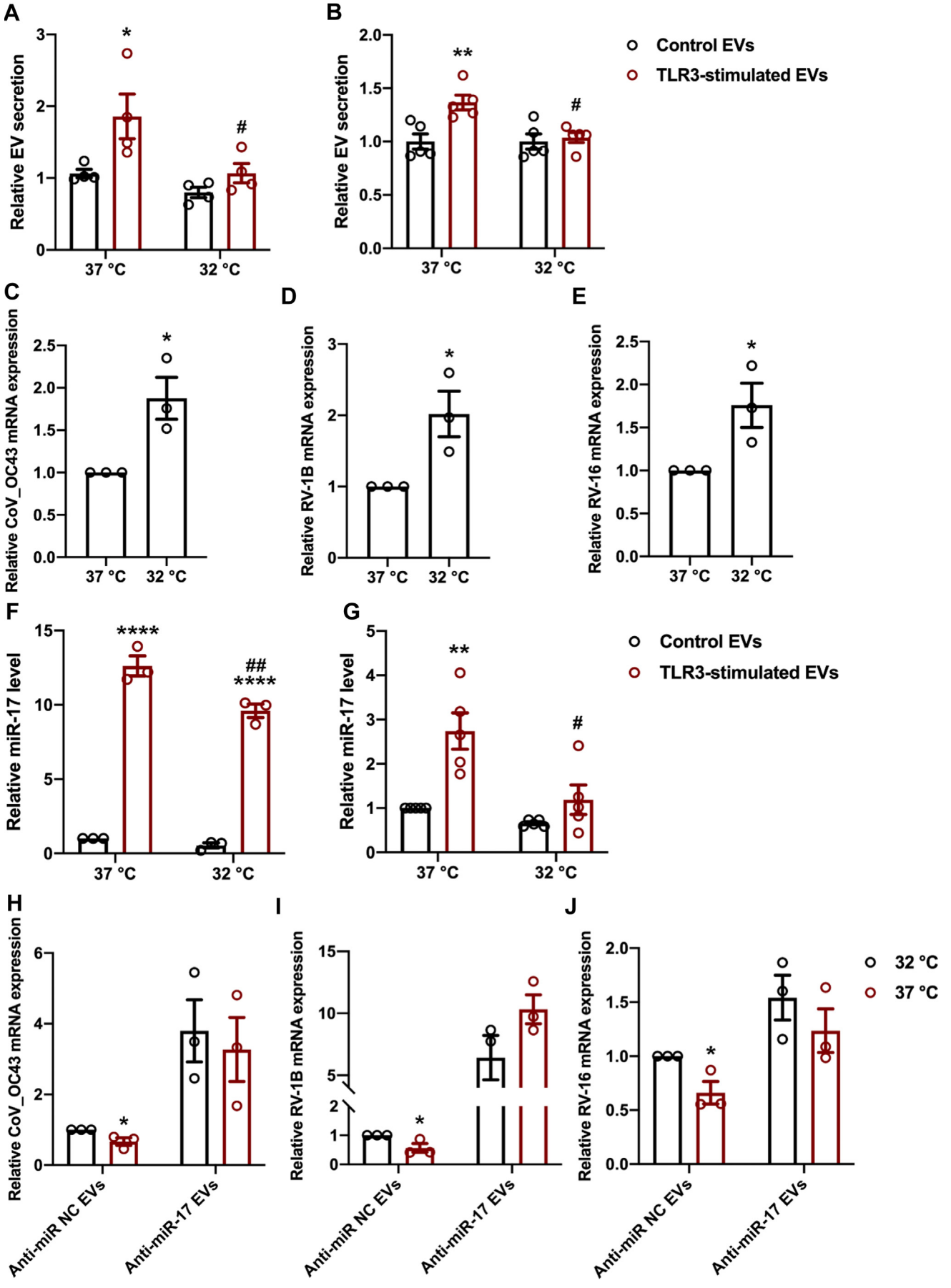
A
Relative EV secretion
37 °C
32 °C
B
Relative EV secretion
Control EVs
TLR3-stimulated EVs
C
Relative CoV_OC43 mRNA expression
D
Relative RV-1B mRNA expression
E
Relative RV-16 mRNA expression
F
Relative miR-17 level
G
Relative miR-17 level
H
Relative CoV_OC43 mRNA expression
Anti-miR NC EVs
Anti-miR-17 EVs
I
Relative RV-1B mRNA expression
J
Relative RV-16 mRNA expression
32 °C
37 °C

Cold exposure impairs TLR3-dependent EV secretion and miR-17 abundance, which abrogates antiviral activity

Next, we analyzed the effect of reduced temperature on TLR3-dependent EV function. We first sought to verify *in vivo* intranasal temperature gradients in healthy human subjects after cold air exposure at the most proximate point of mucosal contact, namely the inferior turbinate. We confirmed that the intranasal temperature at the level of anterior and midinferior turbinate dropped 6.4°C ($P \leq .001$) and 4.7°C ($P \leq .001$) maximum, respectively, after a reduction in ambient temperature from 23.3°C to 4.4°C (see Fig E6 in the Online Repository at www.jacionline.org). We therefore applied a similar reduction of 5°C to the subsequent *in vitro* culture experiments. As shown in Fig 5, *A,* TLR3-stimulated EV secretion was significantly impaired at 32°C relative to 37°C ($P \leq .05$). To validate this result, we repeated the experiment in live human turbinate mucosal tissues, a clinically relevant *ex vivo* model, and found that TLR3 stimulation induced a significant increase in EV secretion at 37°C ($P \leq .01$), while the cool temperature of 32°C significantly impaired TLR3-dependent EV secretion (Fig 5, *B,* $P \leq .05$).

The following set of experiments was designed to further investigate the influence of cold exposure on antiviral activity mediated by TLR3-stimulated EVs with a focus on how miR-17 regulates the temperature-dependent phenotype. As shown in Fig 5, *C-E,* TLR3-stimulated EVs produced at 37°C were more efficient in inhibiting viral infections by CoV_OC43 (Fig 5, *C,* $P \leq .05$), RV-1B (Fig 5, *D,* $P \leq .05$), and RV-16 (Fig 5, *E,* $P \leq .05$) relative to 32°C. We then analyzed the composition of TLR3-stimulated EVs secreted at both temperatures. Fig 5, *F,* reveals that TLR3 stimulation at 37°C significantly increased the expression of miR-17 in EVs compared to the unstimulated control ($P \leq .001$). Incubation at the lower temperature of 32°C significantly diminished the TLR3-dependent miR-17 upregulation ($P \leq .01$). Consistent results were observed when the experiment was performed in live human turbinate mucosal tissues (Fig 5, *G*), demonstrating that the enhancement in EV secretion and antiviral miRNA packaging stimulated through the TLR3 signaling was dependent on the ambient temperature.

Because of the diminished abundance of miR-17 in TLR3-dependent EVs under cold exposure, we next sought to determine whether miR-17 was associated with the temperature-dependent antiviral activity mediated by TLR3-stimulated EVs. As shown in Fig 5, *H-J,* specific knockdown of miR-17 in TLR3-stimulated EVs permitted higher levels of viral infection, particularly at 37°C, and rescued the temperature-dependent phenotype. In addition, exposure to anti–miR-17 EVs produced at 37°C or 32°C did not cause any significant differences in virus mRNA level in host cells ($P > .05$). These results demonstrate that the reduction in antiviral activity of TLR3-stimulated EVs produced at 32°C was strongly correlated with the impaired TLR3-dependent abundance of miR-17 induced by cold exposure.

Cold exposure reduces TLR3-dependent upregulation of EV surface receptor proteins and impairs antiviral activity mediated by surface receptor–virus interactions

In our final set of experiments, we explored how cold exposure affects TLR3-dependent upregulation of EV surface receptor proteins and the antiviral activity mediated by surface receptor–virus interactions. Fig 6 shows that both gene (Fig 6, *A,* $P \leq .005$) and protein (Fig 6, *B,* $P \leq .001$) expression of LDLR in EVs was significantly increased on TLR3 stimulation at 37°C compared to unstimulated controls, while the TLR3-dependent upregulation of LDLR proteins was significantly impaired when EVs were secreted from HNEpCs incubated at 32°C ($P \leq .01$). These results were consistent with the effects of low ambient temperature on TLR3-dependent EV secretion (Fig 5, *A*) and upregulation of miR-17 (Fig 5, *F*). We then repeated this experiment using live human turbinate mucosal tissues and observed similar results (Fig 6, *C*). Likewise, TLR3-dependent upregulation of ICAM-1 in EVs was also significantly diminished by cold exposure in both *in vitro* (Fig 6, *D* and *E*) and *ex vivo* (Fig 6, *F*) settings. Our findings suggest that the enhanced packaging of surface receptor proteins LDLR and ICAM-1 within EVs resulting from TLR3 activation was dependent on ambient temperature.

FIG 5. Cold exposure impairs TLR3-dependent EV secretion and miR-17 abundance, which abrogates antiviral activity. **(A)** Numbers of TLR3-stimulated EVs secreted from HNEpCs at 37°C or 32°C. *$P \leq .05$ for comparison between control and TLR3-stimulated EVs; #$P \leq .05$ for comparison between TLR3-stimulated EVs produced at 37°C and 32°C (2-way ANOVA followed by Tukey test); data represent 4 independent experiments (means ± SEMs). **(B)** Numbers of TLR3-stimulated EVs secreted from human turbinate mucosal explants at 37°C or 32°C. **$P \leq .01$ for comparison between control and TLR3-stimulated EVs; #$P \leq .05$ for comparison between TLR3-stimulated EVs produced at 37°C and 32°C (2-way ANOVA followed by Tukey test); data represent 5 independent experiments (means ± SEMs). **(C-E)** qPCR analysis showing increased virus mRNA levels in HNEpCs infected with CoV_OC43 *(C),* RV-1B *(D),* or RV-16 *(E)* after preincubation with TLR3-stimulated EVs produced at 32°C relative to 37°C. *$P \leq .05$ (2-tailed Student *t* test); data represent 3 independent experiments (means ± SEMs). **(F)** qPCR analysis showing impaired miR-17 upregulation in TLR3-stimulated EVs secreted from HNEpCs at 32°C relative to 37°C. ****$P \leq .001$ for comparison between control and TLR3-stimulated EVs; ##$P \leq .01$ for comparison between TLR3-stimulated EVs produced at 37°C and 32°C (2-way ANOVA followed by Tukey test); data represent 3 independent experiments (means ± SEMs). **(G)** qPCR analysis showing impaired miR-17 upregulation in TLR3-stimulated EVs secreted from human turbinate mucosal explants at 32°C relative to 37°C. **$P \leq .01$ for comparison between control and TLR3-stimulated EVs; #$P \leq .05$ for comparison between TLR3-stimulated EVs secreted at 37°C and 32°C (2-way ANOVA followed by Tukey test); data represent 5 independent experiments (means ± SEMs). **(H-J)** qPCR analysis showing reduced virus mRNA levels in HNEpCs infected with CoV_OC43 *(H),* RV-1B *(I),* or RV-16 *(J)* after preincubation with TLR3-stimulated anti–miR-NC EVs produced at 37°C. Antiviral effect is lost after preincubation with anti–miR-17 EVs produced at 37°C or either EV condition at 32°C. *$P \leq .05$ for comparison between TLR3-stimulated EVs secreted at 37°C and 32°C (2-way ANOVA followed by Tukey test); data represent 3 independent experiments (means ± SEMs).

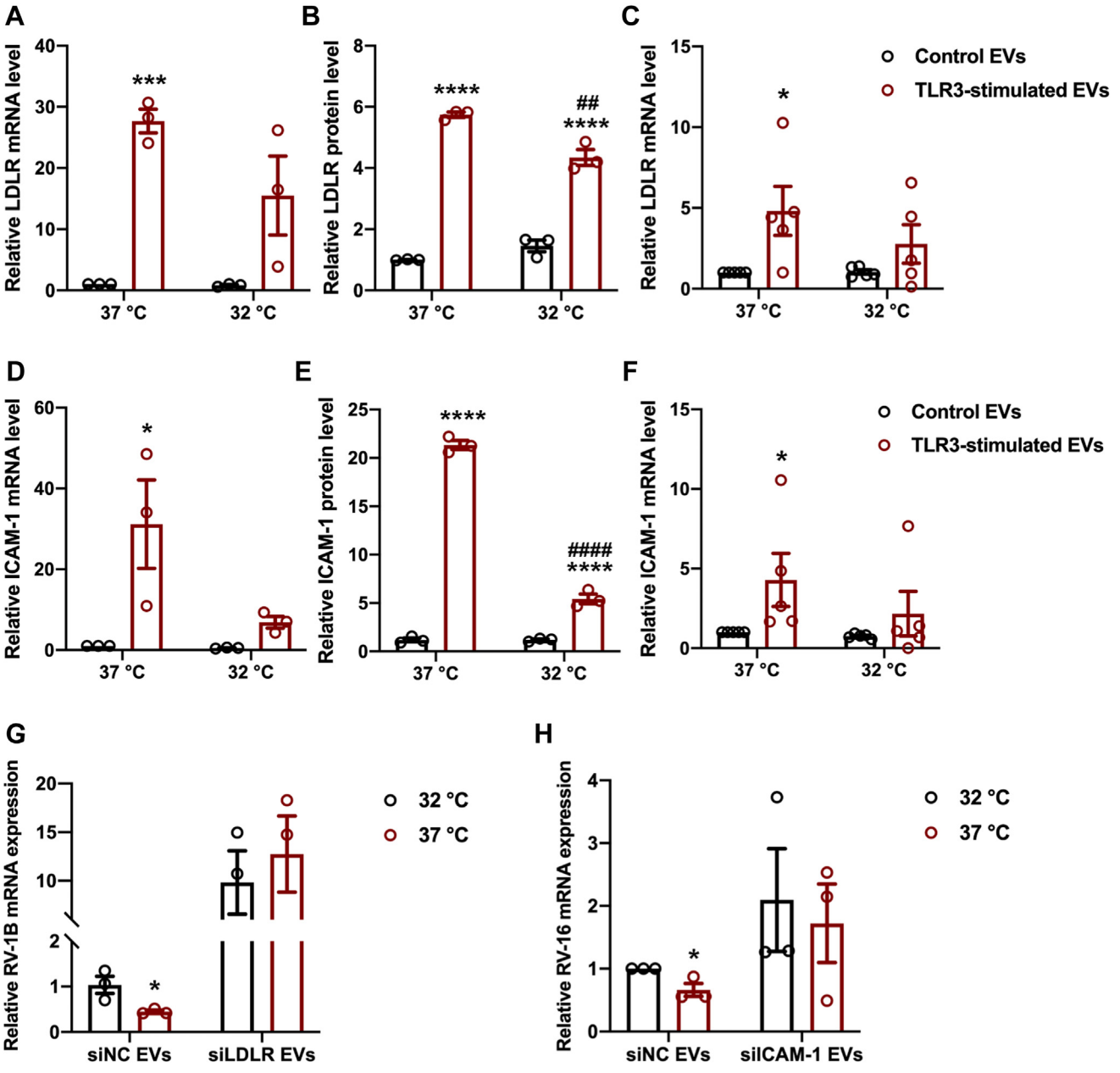

FIG 6. Cold exposure reduces TLR3-dependent upregulation of EV surface receptor proteins and impairs antiviral activity mediated by surface receptor–virus interactions. (**A** and **B**) Reduced LDLR mRNA *(A)* and protein *(B)* levels in TLR3-stimulated EVs secreted from HNEpCs at 32°C relative to 37°C. ****$P \leq .001$ and ***$P \leq .005$ for comparison between control and TLR3-stimulated EVs; ####$P \leq .001$ for comparison between TLR3-stimulated EVs secreted at 37°C and 32°C (2-way ANOVA followed by Tukey test); data represent 3 independent experiments (means ± SEMs). **(C)** qPCR analysis showing reduced LDLR mRNA levels in TLR3-stimulated EVs secreted from human turbinate mucosal explants at 32°C relative to 37°C. *$P \leq .05$ for comparison between control and TLR3-stimulated EVs (2-tailed Student *t* test); data represent 5 independent experiments (means ± SEMs). (**D** and **E**) Reduced ICAM-1 mRNA *(D)* and protein *(E)* levels in TLR3-stimulated EVs secreted from HNEpCs at 32°C relative to 37°C. ****$P \leq .001$ and *$P \leq .05$ for comparison between control and TLR3-stimulated EVs; ####$P \leq .001$ for comparison between TLR3-stimulated EVs secreted at 37°C and 32°C (2-way ANOVA followed by Tukey test); data represent 3 independent experiments (means ± SEMs). **(F)** qPCR analysis showing reduced ICAM-1 mRNA levels in TLR3-stimulated EVs secreted from human turbinate mucosal explants at 32°C relative to 37°C. *$P \leq .05$ for comparison between control and TLR3-stimulated EVs (2-tailed Student *t* test); data represent 5 independent experiments (means ± SEMs). (**G** and **H**) qPCR analysis showing abrogation of reduced virus mRNA levels in HNEpCs infected by RV-1B *(G)*/RV-16 *(H)* after preincubation with TLR3-stimulated siNC EVs at 37°C relative to siLDLR *(G)*/siICAM-1 *(H)* EVs when performed at 32°C. *$P \leq .05$ for comparison between TLR3-stimulated EVs produced at 37°C and 32°C (2-way ANOVA followed by Tukey test); data represent 3 independent experiments (means ± SEMs).

Considering the discovery that TLR3-stimulated EV surface receptor–virus interactions contributed to the antiviral activity and prevented virus entry into host cells, we also explored whether this contribution could be affected by reduced ambient temperature. Fig 6 shows that TLR3-stimulated siNC EVs exhibited significantly enhanced antiviral activities against RV-1B (Fig 6, *G*, $P \leq .05$) and RV-16 (Fig 6, *H*, $P \leq .05$) when produced at 37°C relative to 32°C. The results were consistent with our findings that cold ambient temperature impaired the production of surface receptor proteins within EVs induced by TLR3 stimulation and led to less efficient cargo packaging in EVs (Fig 6, *A-F*). Moreover, the significant reduction in antiviral activity of TLR3-stimulated EVs as a result of the cold ambient temperature was partially eliminated on silencing LDLR (Fig 6, *G*, $P > .05$) or ICAM-1 (Fig 6, *H*, $P > .05$) in EVs, suggesting a robust correlation between temperature-dependent antiviral activity mediated by TLR3-stimulated EVs and packaging of surface receptor proteins within EVs. It bears noting that the decrease in ambient temperature from 37°C to 32°C during preincubation of EVs with viruses did not significantly affect the viral binding affinity and antiviral activity of TLR3-stimulated EVs (see Fig E7 in the Online Repository at www.jacionline.org; $P > .05$).

DISCUSSION

URI is the most frequent manifestation of infectious disease, including the common cold. Seasonal variation in URIs has been well documented, with increased infectious transmission noted during winter.[5,6] Moreover, epidemics caused by respiratory viruses, such as common cold virus, severe acute respiratory syndrome coronavirus (SARS-CoV), and the recent SARS-CoV-2, appear to spike during the colder months. The mechanisms underlying the evident seasonality of respiratory viruses have been debated for many years. Changes in environmental factors and human behavior are the 2 most common arguments. Recent research has highlighted the importance of environmental factors, particularly ambient temperature, in modulating host immune responses to URIs.[9-12,38] However, the biological mechanism underlying the correlation between antiviral host responses and the seasonality of respiratory viruses remains largely unknown.

Our group was the first to discover the innate antibacterial activity of human nasal mucosa–derived EVs. Our previous studies demonstrated that TLR4 activation resulted in a release of EV swarms from the nasal mucosa, which had profound antimicrobial effects within the mucus blanket.[20] Concurrently, other teams have reported that IFN-α induced cell-to-cell transfer of antiviral miRNAs via EVs directed against hepatitis viruses.[39-41] In addition, EVs have been shown to play a role in the pathogenesis of respiratory viral infections, and EV proteins exert direct virion neutralization by binding to virus ligands via surface receptors and block their entry to host cells.[32,42] Collectively, these findings led us to hypothesize a previously unknown role of nasal epithelial EVs in innate antiviral immunity and seasonality of respiratory viral infections. In this conception, TLR3 stimulation induces a swarm-like secretion of nasal epithelial EVs with antiviral activity against respiratory viruses, which is diminished by cold air conditions.

We first studied the role of TLR3 stimulation in regulation of nasal epithelial EV secretion. We used primary HNEpCs isolated from healthy human nasal mucosa to mimic *in vivo* exposure to inhaled respiratory viruses. This is physiologically and clinically relevant, as the mucosa of inferior turbinate within the anterior nasal cavity represents the primary deposition site of inhaled pathogens from the external environment.[43] Poly(I:C), a canonical TLR3 agonist, was used in our study to model generic respiratory viral infection. TLR3 is an established pathway of innate antiviral response to both rhinovirus and coronavirus in airway epithelium.[44,45] We found that poly(I:C) stimulation over 24 hours at a concentration of 2.5 μg/mL resulted in a significant increase in basal EV release rate. The higher dose did not induce a further enhancement due to the accompanied cytotoxicity. The increased EV secretion was regulated by the TLR3 signaling, and IRF3 was involved in the downstream signaling cascade. These findings are consistent with TLR3 as an established pattern recognition receptor capable of rapidly recognizing and responding to virus dsRNA, a pathogen-associated molecular pattern (aka PAMP) associated with RNA viral infections.[46] Using a validated fluorescent tag, we also demonstrated that TLR3-stimulated EVs could be quickly taken up by autologous cells with clathrin-mediated endocytosis involved in EV internalization. The rapid kinetics of intracellular transport supports our hypothesis that EVs secreted from TLR3-stimulated cells in the nasal cavity could transfer their antiviral cargo into neighboring recipient cells and help restore the antiviral state in infected cells before being eliminated by mucociliary clearance.

Next, we explored whether TLR3-stimulated EVs displayed intrinsic antiviral activity against respiratory viruses. We established an infection model in primary HNEpCs with 3 different common respiratory viruses. The viral infectivity in host cells was validated through determination of $TCID_{50}$ and confirmation of successful induction of cytopathic effects as well as host immune responses. We then investigated the antiviral functions mediated by TLR3-stimulated EVs in this infection model. Remarkably, we found potent, broad-spectrum, and dose-dependent antiviral activity of TLR3-stimulated EVs against both coronavirus and rhinovirus. In contrast, exposure to unstimulated control EVs at the same concentration had negligible effects on suppression of viral infection. This relative lack of activity observed among unstimulated EVs further confirms that TLR3 stimulation confers enhanced antiviral properties to the nasal epithelium–derived EVs.

In light of the findings that TLR3-stimulated EVs exerted antiviral activity, we next examined whether TLR3 stimulation was capable of modulating the packaged cargo within EVs and explored an additional role of TLR3-stimulated EVs in viral infection via miRNA transfer to recipient cells. Previous studies have reported that miRNAs in EVs play important regulatory roles in target cells and may be valuable tools for the treatment of certain diseases, including viral infections.[41] To study miRNAs associated with the antiviral effects of TLR3-stimulated EVs, we performed miRNA profiling. We were able to identify a number of differentially expressed miRNAs in TLR3-stimulated EVs relative to unstimulated controls and selected miR-17 for a further investigation because if its validated antiviral roles in URIs.[36,37] We then confirmed that miR-17 had direct antiviral activities against common cold viruses, and its abundance correlated with a proportionate enhancement in antiviral effects of TLR3-stimulated EVs using synthetic mimics and inhibitors. It is commonly believed that miRNAs block virus replication through targeting specific cellular factors or by binding directly to virus genomes.[40,47] Previous studies have shown that miR-17 inhibits human immunodeficiency virus and hepatitis C virus replication through targeting p300/CBP-associated factor (aka PCAF) and

mitogen-activated protein kinase kinase kinase 8 (aka MAP3K8), respectively.[48,49] More recently, miR-17 upregulation as a means of host immune response has been seen during URIs.[50] Studies have also demonstrated that miR-17 targets multiple genomic regions (replicase polyprotein ORF1ab and spike protein) within coronavirus, deactivates virus proteins, and suppresses virus replication.[36,37] However, further studies are needed to understand the detailed antiviral mechanisms of miR-17 against other respiratory viruses, particularly the ones used as model pathogens in our present study.

The next set of experiments was designed to examine a parallel mechanism of TLR3-mediated antiviral defense of EVs through direct binding of mucus-suspended virions. Our studies demonstrate that TLR3 stimulation led to significant abundance of surface receptor proteins in EVs, including LDLR and ICAM-1. TLR3-stimulated EVs thereby functioned in a decoy-like manner by directly binding to rhinovirus and competing with host cell surface LDLR and ICAM-1 to inhibit infection by RV-1B and RV-16, respectively. Although we did not directly explore this effect in this study, it may extend to other respiratory viruses that similarly utilize LDLR or ICAM-1 as their initial tethering receptor. Recent studies have shown that SARS-CoV-2 infections can be blocked by human recombinant soluble angiotensin converting enzyme 2 (ACE2) and even more expeditiously by exosomal ACE2.[32,51] The possible mechanism is that receptor proteins presented on nano-size EVs might amplify the space interval in suppressing virus access to its host cell surface. Moreover, given that a single EV is capable of carrying a broad array of proteins, surface receptor proteins in EVs might possess greater efficiency to block viral infection than receptor proteins in other forms (eg, soluble proteins and protein conjugates), especially in the presence of more than one type of virus.

A major goal of this work was to explore whether antiviral activity of EVs is affected by the cold air conditions typical of seasonal environmental fluctuations. In this study, we confirmed an *in vivo* temperature reduction of approximately 5°C experienced by the nasal cavity in cold ambient environments in healthy human subjects through endoscopically guided measurements. When this nasal temperature reduction was applied to *in vitro* culture, we determined that cold exposure largely impaired the antiviral activity of TLR3-dependent EVs. In addition, the secretion of EVs and abundance of antiviral miR-17 as well as surface receptor proteins LDLR and ICAM-1 that resulted from TLR3 stimulation were greater at the warm temperature of 37°C relative to those at the cool temperature of 32°C. More importantly, the temperature-dependent antiviral effects of TLR3-stimulated EVs were partially abrogated upon silencing these antiviral components in EVs. The confluence of these observations suggests that the potent antiviral functions mediated by TLR3-dependent EVs are impaired by cold air conditions via a 41.9% decrease in total EV release as well as reduced miRNA packaging (23.8%) and antiviral surface receptor binding activity (24.4% and 77.2%) of individual EV.

Similar to our results, a prior study has reported that the antiviral defense response elicited by rhinovirus infection is temperature dependent.[11] Incubating mouse airway cells at the relatively reduced temperature of the nasal cavity during virus replication resulted in lower levels of RIG-I–like receptor, aka RLR, ligand accumulation, impaired RLR function, and decreased IFN responsiveness, leading to less robust antiviral gene expression and restriction of virus. Many respiratory viruses initiate infection in the nasal cavity, which is the first region of contact of inhaled respiratory pathogens and is highly sensitive to changes in ambient air temperature. The diminished innate immune responses to viral infections at cool temperatures could thereby create a more permissive environment for virus replication compared to warm temperatures. These concepts led us to consider the possibility that inhaling cool air in the winter season might impair the antiviral immune defense functions mediated by TLR3-stimulated EVs and decrease resistance to infections by reducing the host cell temperature within the anterior nasal mucosa. Our observations revealed that exposure to cold resulted in increased host susceptibility to respiratory viruses, providing a potential immunologic mechanism for seasonal variation in URIs.

Conclusions

Our findings not only shed light on the role of EV swarms in TLR3-dependent antiviral innate immune responses within the human nasal epithelium but also contribute to our fundamental understanding of the mechanism of seasonal variation in URI prevalence. We have shown that activation of nasal epithelial TLR3 by inhaled respiratory viruses leads to increased secretion of EVs with an abundance of antiviral components, including miR-17, LDLR, and ICAM-1. The EV swarms exhibit potent antiviral activity and protect the host from infection through transfer of antiviral miRNAs and direct binding of mucus-suspended virions. Moreover, these functions are impaired by cold exposure via a reduction in total EV secretion and diminished miRNA packaging as well as antiviral binding affinity of individual EV. Lending particular strength to our conclusions was that we were able to investigate the mechanisms of EV-mediated antiviral innate immune defense in primary human epithelial cells and to corroborate *in vitro* data with live human nasal mucosal tissues taken from fresh surgical specimens. EVs have been utilized as drug delivery systems with therapeutic potential against various diseases. We speculate that the therapeutic efficacy of nasal epithelial EVs can be further potentiated through codelivery of additional antiviral agents. Integration of EVs and antiviral agents may allow us to develop new treatments for respiratory viral infections and reduce the potential adverse effects from both therapeutics.

We thank Philip Seifert (Schepens Eye Research Institute of Massachusetts Eye and Ear Infirmary) for his technical expertise and mentoring in immunogold TEM. We also thank the Institute for Chemical Imaging of Living Systems at Northeastern University for consultation and imaging support.

Key messages

- **Nasal epithelial EVs participate in TLR3-dependent antiviral immunity.**
- **Nasal epithelial EVs protect the host from respiratory viral infections through functional delivery of miRNAs and direct virion neutralization.**
- **Cold exposure impairs antiviral immune defense functions mediated by nasal epithelial EVs.**

REFERENCES

1. Bertino JS. Cost burden of viral respiratory infections: issues for formulary decision makers. Am J Med 2002;112:42-9.
2. Winther B. Rhinovirus infections in the upper airway. Proc Am Thorac Soc 2011; 8:79-89.
3. Bosch AATM, Biesbroek G, Trzcinski K, Sanders EAM, Bogaert D. Viral and bacterial interactions in the upper respiratory tract. PLoS Pathog 2013;9:e1003057.
4. Taubenberger JK, Kash JC. Influenza virus evolution, host adaptation, and pandemic formation. Cell Host Microbe 2010;7:440-51.
5. Sloan C, Moore ML, Hartert T. Impact of pollution, climate, and sociodemographic factors on spatiotemporal dynamics of seasonal respiratory viruses. Clin Transl Sci 2011;4:48-54.
6. Conlon KC, Rajkovich NB, White-Newsome JL, Larsen L, O'Neill MS. Preventing cold-related morbidity and mortality in a changing climate. Maturitas 2011;69: 197-202.
7. Tanner LM, Moffatt S, Milne EMG, Mills SDH, White M. Socioeconomic and behavioural risk factors for adverse winter health and social outcomes in economically developed countries: a systematic review of quantitative observational studies. J Epidemiol Community Health 2013;67:1061-7.
8. Papadopoulos NG, Sanderson G, Hunter J, Johnston SL. Rhinoviruses replicate effectively at lower airway temperatures. J Med Virol 1999;58:100-4.
9. Ikäheimo TM, Jaakkola K, Jokelainen J, Saukkoriipi A, Roivainen M, Juvonen R, et al. A decrease in temperature and humidity precedes human rhinovirus infections in a cold climate. Viruses 2016;8:244.
10. Jaakkola K, Saukkoriipi A, Jokelainen J, Juvonen R, Kauppila J, Vainio O, et al. Decline in temperature and humidity increases the occurrence of influenza in cold climate. Environ Health 2014;13:22.
11. Foxman EF, Storer JA, Fitzgerald ME, Wasik BR, Hou L, Zhao H, et al. Temperature-dependent innate defense against the common cold virus limits viral replication at warm temperature in mouse airway cells. Proc Natl Acad Sci U S A 2015; 112:827-32.
12. Foxman EF, Storer JA, Vanaja K, Levchenko A, Iwasaki A. Two interferon-independent double-stranded RNAinduced host defense strategies suppress the common cold virus at warm temperature. Proc Natl Acad Sci U S A 2016;113:8496-501.
13. Noback ML, Harvati K, Spoor F. Climate-related variation of the human nasal cavity. Am J Phys Anthropol 2011;145:599-614.
14. Kaliner MA. Human nasal host defense and sinusitis. J Allergy Clin Immunol 1992;90:424-30.
15. Antunes MB, Cohen NA. Mucociliary clearance—a critical upper airway host defense mechanism and methods of assessment. Curr Opin Allergy Clin Immunol 2007;7:5-10.
16. Kojima T, Go M, Takano KI, Kurose M, Ohkuni T, Koizumi JI, et al. Regulation of tight junctions in upper airway epithelium. Biomed Res Int 2013;2013.
17. Schleimer RP, Kato A, Kern R, Kuperman D, Avila PC. Epithelium: at the interface of innate and adaptive immune responses. J Allergy Clin Immunol 2007;120:1279-84.
18. Lester SN, Li K. Toll-like receptors in antiviral innate immunity. J Mol Biol 2014; 426:1246-64.
19. Sen GC, Sarkar SN. Transcriptional signaling by double-stranded RNA: role of TLR3. Cytokine Growth Factor Rev 2005;16:1-14.
20. Nocera AL, Mueller SK, Stephan JR, Hing L, Seifert P, Han X, et al. Exosome swarms eliminate airway pathogens and provide passive epithelial immunoprotection through nitric oxide. J Allergy Clin Immunol 2019;143:1525-35.e1.
21. Wu M, Ouyang Y, Wang Z, Zhang R, Huang PH, Chen C, et al. Isolation of exosomes from whole blood by integrating acoustics and microfluidics. Proc Natl Acad Sci U S A 2017;114:10584-9.
22. Mueller SK, Nocera AL, Bleier BS. Exosome function in aerodigestive mucosa. Nanomedicine 2018;14:269-77.
23. Kalluri R, LeBleu VS. The biology, function, and biomedical applications of exosomes. Science 2020;367:eaau6977.
24. Anderson MR, Kashanchi F, Jacobson S. Exosomes in viral disease. Neurotherapeutics 2016;13:535-46.
25. Mills JT, Schwenzer A, Marsh EK, Edwards MR, Sabroe I, Midwood KS, et al. Airway epithelial cells generate pro-inflammatory tenascin-C and small extracellular vesicles in response to *TLR3* stimuli and rhinovirus infection. Front Immunol 2019;10:1987.
26. Kouwaki T, Fukushima Y, Daito T, Sanada T, Yamamoto N, Mifsud EJ, et al. Extracellular vesicles including exosomes regulate innate immune responses to hepatitis B virus infection. Front Immunol 2016;7:335.
27. Maemura T, Fukuyama S, Sugita Y, Lopes TJS, Nakao T, Noda T, et al. Lung-derived exosomal miR-483-3p regulates the innate immune response to influenza virus infection. J Infect Dis 2018;217:1372-82.
28. Taft RJ, Pang KC, Mercer TR, Dinger M, Mattick JS. Non-coding RNAs: regulators of disease. J Pathol 2010;220:126-39.
29. Hu G, Zhou R, Liu J, Gong AY, Chen XM. MicroRNA-98 and let-7 regulate expression of suppressor of cytokine signaling 4 in biliary epithelial cells in response to *Cryptosporidium parvum* infection. J Infect Dis 2010;202: 125-35.
30. Wu W, Wu D, Yan W, Wang Y, You J, Wan X, et al. Exosomes with miR-574 transfer anti-HBV activity mediated by the interferon from macrophage to HBV-infected hepatocyte. J Infect Dis 2021;223:686-98.
31. Jung YJ, Kim JW, Park SJ, Min BY, Jang ES, Kim NY, et al. c-Myc–mediated overexpression of miR-17-92 suppresses replication of hepatitis B virus in human hepatoma cells. J Med Virol 2013;85:969-78.
32. El-Shennawy L, Hoffmann AD, Dashzeveg NK, McAndrews KM, Mehl PJ, Cornish D, et al. Circulating ACE2-expressing extracellular vesicles block broad strains of SARS-CoV-2. Nat Commun 2022;13:405.
33. Bleier BS, Mulligan RM, Schlosser RJ. Primary human sinonasal epithelial cell culture model for topical drug delivery in patients with chronic rhinosinusitis with nasal polyposis. J Pharm Pharmacol 2012;64:449-56.
34. Théry C, Amigorena S, Raposo G, Clayton A. Isolation and characterization of exosomes from cell culture supernatants and biological fluids. Curr Protoc Cell Biol 2006;30:3-22.
35. Alexopoulou L, Holt AC, Medzhitov R, Flavell RA. Recognition of double-stranded RNA and activation of NF-κB by Toll-like receptor 3. Nature 2001; 413:732-8.
36. Khan MAAK, Sany MRU, Islam MS, Islam ABMMK. Epigenetic regulator miRNA pattern differences among SARS-CoV, SARS-CoV-2, and SARS-CoV-2 world-wide isolates delineated the mystery behind the epic pathogenicity and distinct clinical characteristics of pandemic COVID-19. Front Genet 2020; 11:765.
37. Mallick B, Ghosh Z, Chakrabarti J. MicroRNome analysis unravels the molecular basis of SARS infection in bronchoalveolar stem cells. PLoS One 2009;4:e7837.
38. Moriyama M, Hugentobler WJ, Iwasaki A. Seasonality of respiratory viral infections. Annu Rev Virol 2020;7:83-101.
39. Li J, Liu K, Liu Y, Xu Y, Zhang F, Yang H, et al. Exosomes mediate the cell-to-cell transmission of IFN-α–induced antiviral activity. Nat Immunol 2013;14:793-803.
40. Wu W, Wu D, Yan W, Wang Y, You J, Wan X, et al. Interferon-induced macrophage-derived exosomes mediate antiviral activity against hepatitis B virus through miR-574-5p. J Infect Dis 2021;223:686-98.
41. Qian X, Xu C, Fang S, Zhao P, Wang Y, Liu H, et al. Exosomal microRNAs derived from umbilical mesenchymal stem cells inhibit hepatitis C virus infection. Stem Cells Transl Med 2016;5:1190-203.
42. Krishnamachary B, Cook C, Kumar A, Spikes L, Chalise P, Dhillon NK. Extracellular vesicle–mediated endothelial apoptosis and EV-associated proteins correlate with COVID-19 disease severity. J Extracell Vesicles 2021; 10:e12117.
43. Patki A, Frank-Ito DO. Characterizing human nasal airflow physiologic variables by nasal index. Respir Physiol Neurobiol 2016;232:66-74.
44. Sajjan US, Jia Y, Newcomb DC, Bentley JK, Lukacs NW, LiPuma JJ, et al. *H influenzae* potentiates airway epithelial cell responses to rhinovirus by increasing ICAM-1 and TLR3 expression. FASEB J 2006;20:2121-3.
45. Lévy R, Bastard P, Lanternier F, Lecuit M, Zhang SY, Casanova JL. IFN-α2a therapy in two patients with inborn errors of *TLR3* and *IRF3* infected with SARS-CoV-2. J Clin Immunol 2021;41:26-7, Erratum in: J Clin Immunol 2021;41:28.
46. Chen N, Xia P, Li S, Zhang T, Wang TT, Zhu J. RNA sensors of the innate immune system and their detection of pathogens. IUBMB Life 2017;69:297-304.
47. Lee CH, Kim JH, Lee SW. The role of microRNAs in hepatitis C virus replication and related liver diseases. J Microbiol 2014;52:445-51.
48. Triboulet R, Mari B, Lin YL, Chable-Bessia C, Bennasser Y, Lebrigand K, et al. Suppression of microRNA-silencing pathway by HIV-1 during virus replication. Science 2007;315:1579-82.
49. Tsubota A, Mogushi K, Aizaki H, Miyaguchi K, Nagatsuma K, Matsudaira H, et al. Involvement of MAP3K8 and miR-17-5p in poor virologic response to interferon-based combination therapy for chronic hepatitis C. PLoS One 2014; 9:e97078.
50. Zhu Z, Qi Y, Ge A, Zhu Y, Xu K, Ji H, et al. Comprehensive characterization of serum microRNA profile in response to the emerging avian influenza A (H7N9) virus infection in humans. Viruses 2014;6:1525-39.
51. Monteil V, Kwon H, Prado P, Hagelkrüys A, Wimmer RA, Stahl M, et al. Inhibition of SARS-CoV-2 infections in engineered human tissues using clinical-grade soluble human ACE2. Cell 2020;181:905-13.e7.

METHODS

Temperature measurement of human nasal cavity

Four healthy volunteers were recruited with a total of 8 nasal cavities measured. Exclusion criteria included history of nasal obstruction, nasal surgery, smoking, asthma, symptoms of cold or sinus infection, immunodeficiency, or current fever. The nasal mucosal temperature measurement protocol was adapted from previous studies.[E1,E2] Before measurement, all subjects spent 15 minutes acclimating to ambient temperature (23.3°C) and humidity (57%), breathing quietly while upright. Nasal mucosal temperature was measured with a thermocouple wire probe (mini–Type K, thermocouple thermoelectric wire consisting of chromel and alumel; Reed Instruments, Lake Forest, Ill) coupled to a thermocouple thermometer (mini–Type K, Extech Instruments, Lake Forest, Ill) used for temperature recording. The system was calibrated and NIST certified (FLIR Systems, Nashua, NH) to ±0.3% reading + 1°C accuracy in the range of −93 to 1000°C. Temperature measurements were performed by placing the thermocouple gently on the nasal mucosal surface. The volunteer's head was fixed, and the sensor was consecutively positioned in the nasal valve area close to the head of the inferior turbinate and midinferior turbinate. The sensor was inserted into the nasal cavity under direct endoscopic visualization by a trained otolaryngologist to ensure anatomic-site and technique consistency between subjects. The nasal cavity of each volunteer was examined without decongestion or topical anesthesia. The mucosal temperatures at each site of the nasal cavity were recorded for 30 seconds without interruption of nasal breathing.

Subsequently, all subjects were exposed to cold temperature (4.4°C) and humidity (90%) for 15 minutes, breathing quietly while upright. A new measurement cycle was then performed, respecting the same conditions described for thermocouple placement. No mucosal irritation due to the thermocouple contact was visualized. To ensure proper environmental conditions, simultaneous relative humidity and temperature detection was measured by a calibrated indoor thermometer and humidity monitor (AcuRite Pro, Lake Forest, Ill). Therefore, relative humidity between 1% and 99% could be evaluated. The monitor had a humidity accuracy of ±2% relative humidity and a temperature accuracy of ±0.3°C.

REFERENCES

E1. Bailey RS, Casey KP, Pawar SS, Garcia GJM. Correlation of nasal mucosal temperature with subjective nasal patency in healthy individuals JAMA Facial Plast Surg 2017;19:46-52.

E2. Lindemann J, Keck T, Scheithauer MO, Leiacker R, Wiesmiller K. Nasal mucosal temperature in relation to nasal airflow as measured by rhinomanometry Am J Rhinol 2007;21:46-9.

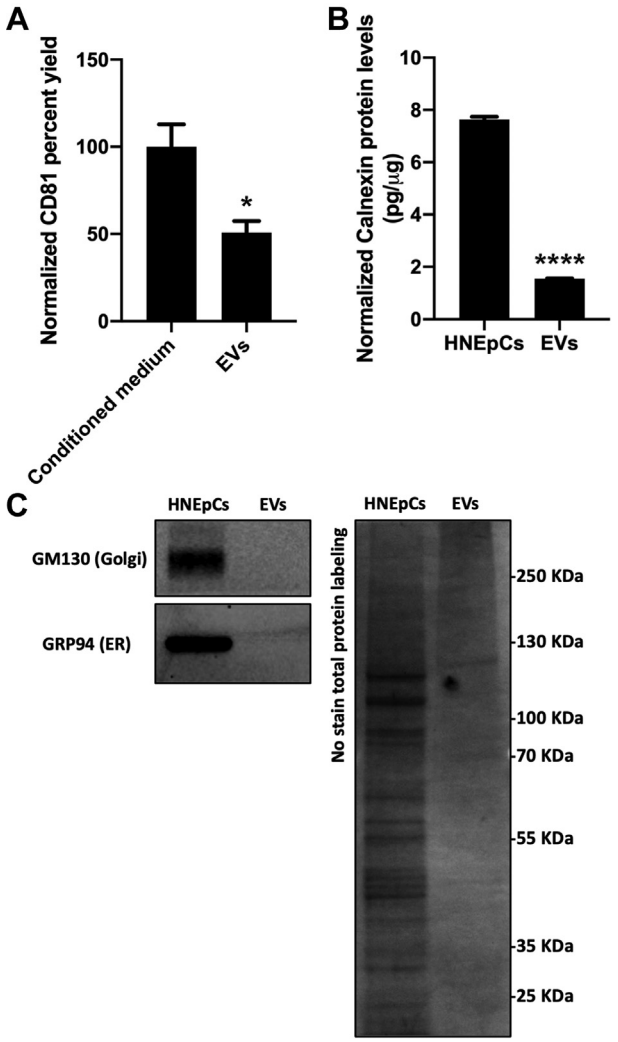

FIG E1. Validation of EV isolation and purification procedures. **(A)** EV isolation yield measured with a CD81 exosome ELISA complete kit (System Biosciences). **(B)** EV purity measured with a calnexin ELISA kit (MyBiosource, San Diego, Calif). All values were normalized to total protein concentration within the same sample with a Pierce BCA protein assay kit (Thermo Fisher). $*P \leq .05$ and $****P \leq .001$ (2-tailed Student *t* test); data represent 3 independent experiments (means ± SEMs). **(C)** Western blot analysis showing GM130 and GRP94 protein expression in HNEpC-derived EVs and cell lysates as well as loading control of the membrane proteins labeled with a No-Stain protein labeling reagent (Thermo Fisher).

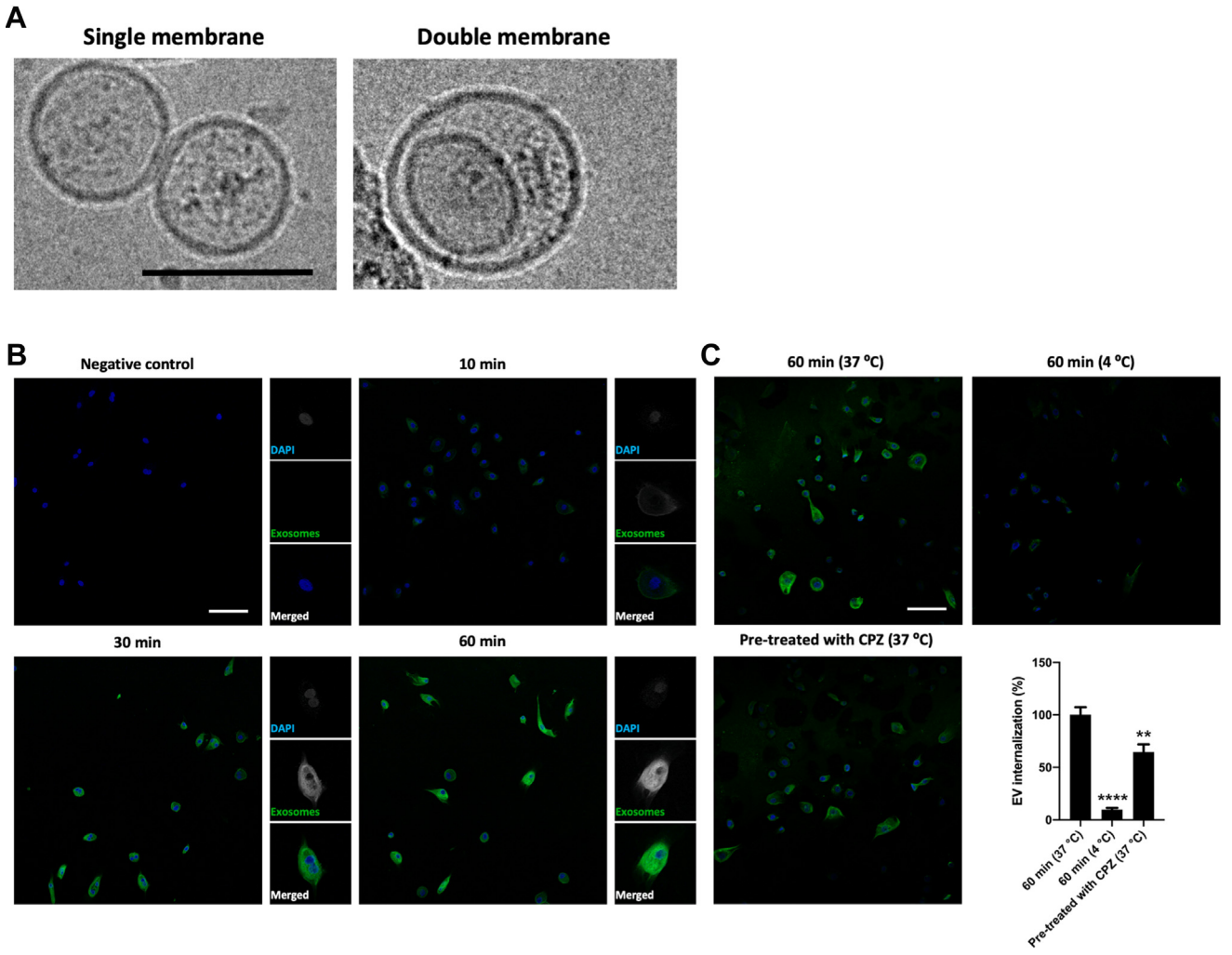

FIG E2. Characterization of control EVs secreted from HNEpCs without TLR3 stimulation. **(A)** Representative cryogenic electron microscopic images of EVs secreted from HNEpCs without TLR3 stimulation (unstimulated control EVs); scale bar = 100 nm. **(B)** Representative confocal microscopic images of fluorescent dye–labeled control EV uptake in HNEpCs over 60 minutes; scale bar = 100 μm. **(C)** Representative confocal microscopic images of fluorescent dye–labeled control EV uptake in HNEpCs for 60 minutes in different conditions (37°C vs 4°C and with or without pretreatment of clathrin-mediated endocytosis inhibitor (chlorpromazine [CPZ], 25 μmol) and quantitative analysis of corrected fluorescence integrated density indicating percentage of EV internalization in HNEpCs; scale bar = 100 μm. $^{****}P \leq .001$ and $^{**}P \leq .01$ (1-way ANOVA followed by Tukey test); data represent 3 independent experiments (means ± SEMs).

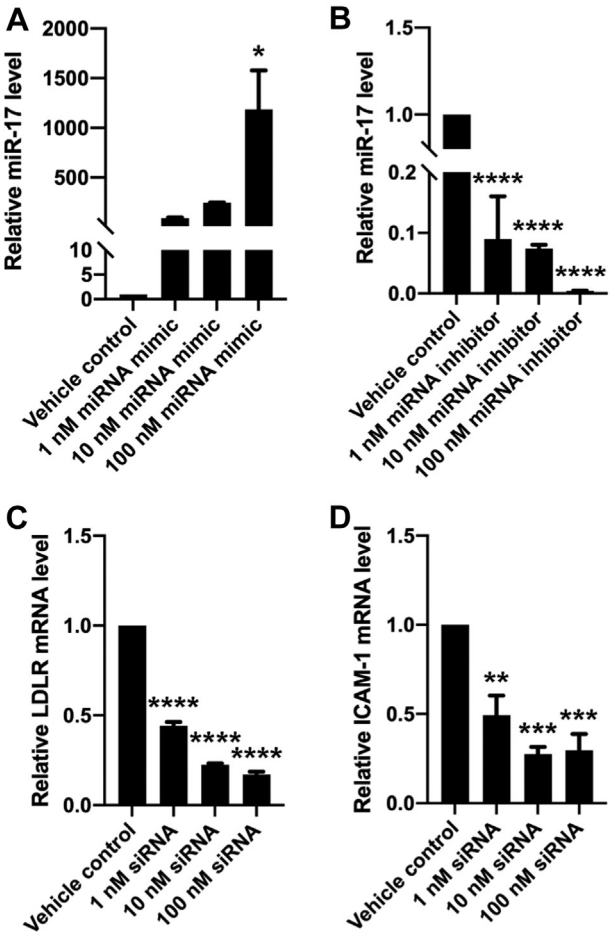

FIG E3. Dose responses in RNA expression levels in HNEpCs transfected with RNA interference tools. (**A** and **B**) qPCR analysis showing miR-17 levels in HNEpCs transfected with miR-17 mimic *(A)* and inhibitor *(B)* at concentrations ranged from 1 nmol to 100 nmol. (**C** and **D**) qPCR analysis showing LDLR *(C)* and ICAM-1 *(D)* mRNA levels of HNEpCs transfected with LDLR *(C)* and ICAM-1 *(D)* siRNA at concentrations that ranged from 1 to 100 nmol. ****$P \leq .001$, ***$P \leq .005$, **$P \leq .01$, and *$P \leq .05$ (1-way ANOVA followed by Tukey test); data represent 3 independent experiments (means ± SEMs).

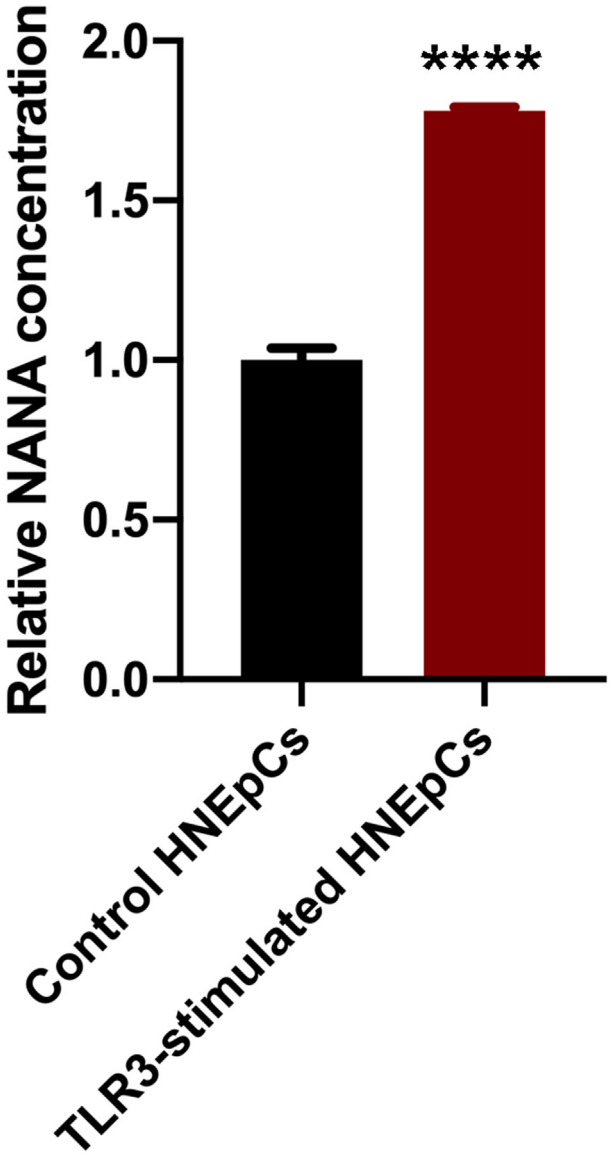

FIG E4. Quantification of intracellular NANA levels. The amount of intracellular NANA with or without TLR3 stimulation was quantified with a sialic acid assay kit (Sigma-Aldrich). ****$P \leq .001$ (2-tailed Student *t* test); data represent 3 independent experiments (means ± SEMs).

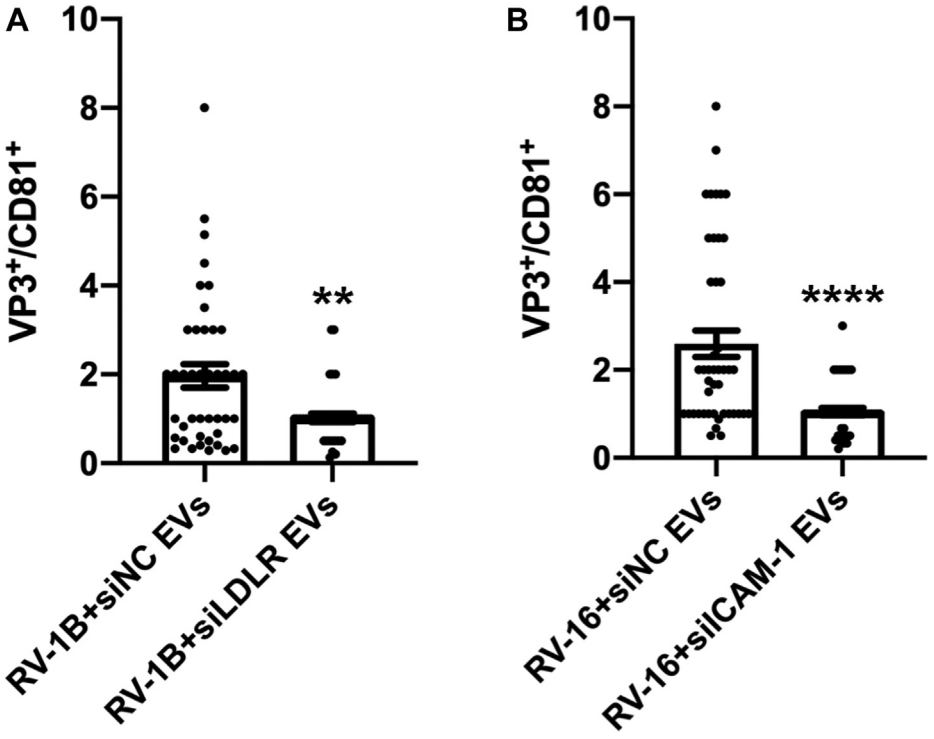

FIG E5. Quantification of TEM images of TLR3-stimulated EVs with immunogold labeling. **(A)** Quantification of the ratio of number of 10 nm nanogold particles ($VP3^+$ RV-1B) to number of 15 nm nanogold particles ($CD81^+$ exosomes); 42 double-positive ($VP3^+/CD81^+$) clusters were analyzed for each group. $^{**}P \leq .01$ (2-tailed Student *t* test). **(B)** Quantification of the ratio of number of 10 nm nanogold particles ($VP3^+$ RV-16) to number of 15 nm nanogold particles ($CD81^+$ EVs); 47 double-positive ($VP3^+/CD81^+$) clusters were analyzed for each group. $^{****}P \leq .001$ (2-tailed Student *t* test).

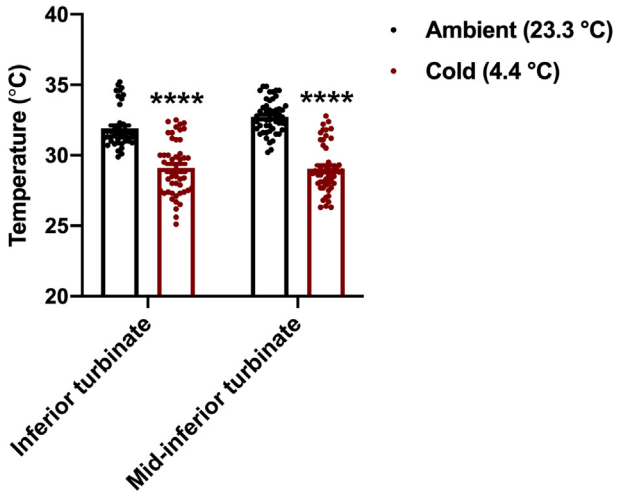

FIG E6. Temperature of nasal mucosa in healthy human volunteers. Intranasal temperature measured in healthy human volunteers in an ambient (23.3°C) or cold (4.4°C) environment. ****$P \leq .001$ (2-tailed Student *t* test); data represent 4 independent experiments (means ± SEMs).

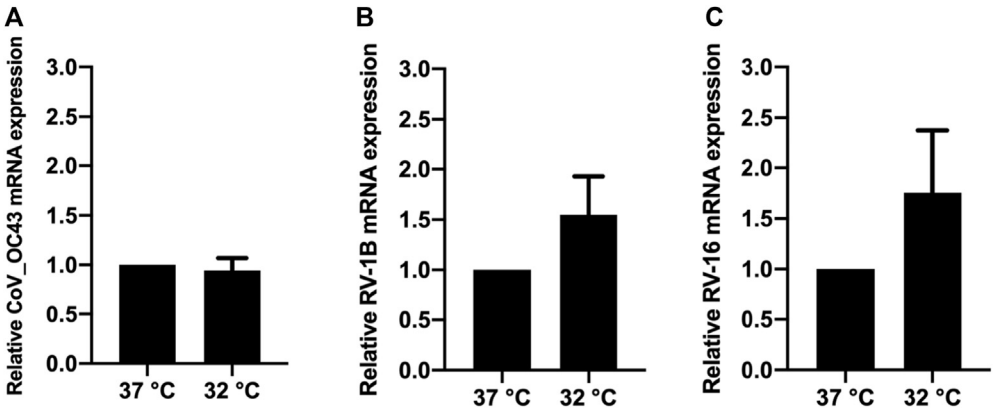

FIG E7. Impact of pre-incubation temperature on the antiviral activity of TLR3-stimulated EVs mediated by surface receptor-viral interactions. Real-time qPCR analysis showing comparable viral mRNA levels in HNEpCs infected by CoV_OC43 **(A)**, RV-1B **(B)**, and RV-16 **(C)** following pre-incubation at 37 °C or 32 °C with TLR3-stimulated EVs produced at 37 °C; $P > .05$ (2-tailed Student *t*-test). Data shown in this figure represent 3 independent experiments (mean ± SEM).